# A *TranSNP* in the DDIT4 mRNA can impact its translation efficiency and modulate p53-dependent responses in cancer cells

Meriem Hadjer Hamadou*[1], Laura Alunno*[1], Tecla Venturelli[1,2], Samuel Valentini[2], Davide Dalfovo[2], Francesca Lorenzini[3], Alessia Mattivi[4], Vincenza Vigorito[4], Glenda Paola Grupelli[5], Alessandro Matte'[6], Pamela Gatto[7], Michael Pancher[7], Chiara Valentini[8], Veronica De Sanctis[8], Roberto Bertorelli[8], Virginie Marcel[9], Emilio Cusanelli[5], Stefano Freddi[10,11], Giovanni Bertalot[12], Sara Zaccara[13], Marina Mione[3], Luca L. Fava[4], Alessandro Romanel[#2], Alberto Inga[#1]

[1] Laboratory of Transcriptional Networks; [2] Laboratory of Bioinformatics and Computational Genomics; [3] Laboratory of Experimental Biology;[4] Armenise-Harvard Laboratory of Cell Division; [5] Cell Biology and Molecular Genetics Laboratory; [6] Cell Analysis and Separation Core Facility; [7] High-Throughput Screening Core Facility; [8] Next Generation Sequencing (NGS) Core Facility; Department of Cellular, Computational, and Integrative Biology, CIBIO, University of Trento, Trento, Italy
[9] Ribosome, Translation and Cancer » team, Centre de Recherche en Cancérologie de Lyon (CRCL), INSERM U1052, CNRS UMR5286, Centre Léon Bérard, Université de Lyon, Université Claude Bernard Lyon 1, 69008, Lyon, France
[10] Department of Oncology and Hematology-Oncology, Università degli Studi di Milano, Milan, Italy
[11] IEO, European Institute of Oncology IRCCS, Milan, Italy
[12] Unità Operativa Multizonale di Anatomia Patologica, APSS, Trento, Italy, Centre for Medical Sciences – CISMed, University of Trento, Italy
[13] Department of Systems Biology, Columbia University Irving Medical Center, NY, USA

*equal first authors
#equal last and corresponding authors

**Keywords**
Polysome-profiling; translation; DDIT4, mTOR, p53, ER-stress

**Abstract**

Relatively few studies have examined the link between SNPs and mRNA translation, despite the established importance of translational regulation in shaping cell phenotypes. We developed a pipeline analyzing the allelic imbalance in total and polysome-bound mRNAs from paired RNA-seq data of HCT116 cells and identified 40 candidate *tranSNPs*, i.e. SNPs associated with allele-specific translation. Among them, the SNP rs1053639 (T/A) on DNA damage-inducible transcript 4 (DDIT4) 3'UTR was identified, with the reference T allele showing a higher polysome association. rs1053639 TT clones generated by genome editing exhibited significantly higher DDIT4 protein levels than AA ones. The difference in DDIT4 proteins was even greater when cells were treated with Thapsigargin or Nutlin, two perturbations that induce DDIT4 transcription. The RNA binding protein RBMX influenced this allele-dependent differences in DDIT4 protein expression, as shown by RNA-EMSA, RIP, and smiFISH assays. RBMX depletion reduced DDIT4 protein in TT clones to the AA levels. Functionally, TT clones more effectively repressed mTORC1 under ER stress, while AA clones outcompeted TT clones in vitro or when injected in zebrafish embryos. The rs1053639 AA genotype, under a recessive model, correlates with poor prognosis in TCGA cancer data.

## Introduction

Many studies in the last decade have demonstrated the importance of translational regulation in shaping cell phenotype (Xu and Ruggero 2020; Schafer et al. 2015; Fujii et al. 2017; Robichaud et al. 2019). Instead, relatively few studies focused on the identification and characterization of genetic variants impacting directly on mRNA translation, although allele-specific expression finely modulating epigenetic and transcriptional regulation has been revealed as critical for many pathophysiological processes (De La Chapelle 2009; St. Pierre et al. 2022; Lee et al. 2019; Przytycki and Singh 2020). To investigate instances of allele-specific mRNA translation efficiency, we recently developed a method that focuses on single nucleotide polymorphisms (SNP) and integrates information from SNP genotyping with RNA-seq data performed on both total and polysome-bound mRNAs (Valentini et al. 2021). Briefly, heterozygous SNPs mapped by genotyping assays are followed in RNA-seq data by calculating allelic fractions (AFs) for both total and polysomal RNA. Coverage threshold, consistency among biological replicates, and the differences in AF between paired total and polysomal RNA samples are used to nominate candidate tranSNPs. The method assumes that the translatome, defined as the ensemble of transcripts that co-sediment with polysomes on sucrose gradients, represents a proxy for the proteome (Pringle et al. 2019). Also, it assumes that if two alleles expressed by a cell can be distinguished due to heterozygous SNPs or other types of variants, a difference in their relative abundance within the polysomes would signal an instance of allele-specific difference in translation efficiency. Hence, the name tranSNPs is attributed to the variants emerging from our pipeline (Valentini et al. 2021). Besides polysomal profiling, Ribo-seq is another approach typically used to characterize the translatome. The method can reach a single-nucleotide positional resolution of the ribosomes along a transcript. The polysome-seq variant protocol could be potentially applied to our scope, as 80S monosomes, whose actual translational status is still somewhat debated (Heyer and Moore 2016), are removed before processing the samples by RNAse treatment to retrieve ribosome-protected fragments (Clamer et al. 2018). However, we decided to use polysomal profiling to increase the possibility of obtaining robust coverage also in 5'- and 3'-UTR regions of mRNAs. Our earlier study identified 147 tranSNPs, corresponding to about 4% of analyzable SNPs in a dataset obtained in the MCF7 cancer cell lines. Of those, 39 were located in the 3'UTR (Valentini et al. 2021) and could impact, directly or through structural features, the binding of trans-factors that, in turn, can affect translation efficiency or mRNA stability.

We have now extended our analysis using data produced in the HCT116 p53 wild-type cell line cultured in control conditions or treated with the MDM2 inhibitor Nutlin (Rizzotto et al. 2020). While tranSNPs could potentially impact multiple cellular phenotypes and outcomes, we decided to continue to focus on a non-genotoxic p53-activating treatment in cancer cells due to profound changes in mRNA translation in cancer (Robichaud et al. 2019), and the growing evidence linking the tumor suppressor p53 to various features of mRNA translation control. For example, p53 was shown to modulate eIF4EBP1, mTORC1, and Endoplasmic Reticulum (ER) stress (Marcel et al.

2018, 2013; Tiu et al. 2021), and, through the modulation of Ribosomal Proteins (RBPs) and microRNAs, to impact the fate of specific sets of mRNAs (Zhang and Chen 2008; He et al. 2007; Marcel et al. 2015). We identified 40 candidate tranSNPs, corresponding to about 7% of analyzable SNPs. Among these tranSNP candidates, four were prioritized for validation experiments considering minor allele frequency, the relevance of the associated genes in cancer, the position along the gene sequence, and the presence of predictions for overlapping trans factor binding sites. One candidate, rs1053639 T/A in the 3'UTR of the DDIT4 (REDD1, RTP801) gene, caught our particular interest. DNA damage-inducible transcript 4 DDIT4 is a negative modulator of mTORC1, is an established target of p53, RFX7, and ATF4, and acts as a tumor suppressor gene (Coronel et al. 2022; Sofer et al. 2005). We generated HCT116 cell line trios for rs1053639 exploiting a CRISPR/Cas9-mediated knock-in strategy (Ghetti et al. 2021) starting from the heterozygous (AT) parental cells. Homozygous TT and AA cell clones were characterized, which revealed differences in DDIT4 protein expression both in basal and induced conditions, alterations in the relative expression of mTOR markers, and changes in mRNA subcellular localization and translatability. Mechanistically, we implicated the RNA binding protein RBMX in a distinct fate of DDIT4 mRNA for rs1053639 alleles. We also established higher relative proliferation and fitness for A-homozygous cells in both *in vitro* and xenograft experiments in zebrafish embryos and explored the correlation between rs1053639 alleles and DDIT4 protein expression in primary tumor samples and the prognostic value of this SNP using TCGA data.

## Results

### TranSNPs can be identified in mock and Nutlin-treated HCT116 cells

Single-end RNA-seq data obtained from HCT116 cells under either mock or 10 μM Nutlin treatment for 16 hours were processed starting from row files by trimming, aligning, and deduplication steps (see Methods). SNPs in exonic and UTR regions were extracted from dbSNP. A list of heterozygous SNPs was compiled based on AF values between 0.2 and 0.8 in at least one of the four replicates in one of the two fractions sequenced (total and polysomal RNA), setting a minimal threshold of 20 reads for AF calculations (**Figure S1**). In addition, only the SNPs with AF measures available for all four biological replicates, the two fractions, and across the two treatments were considered to calculate changes in AF between the fractions (N= 582, **Table S1**). For each SNP, we exploited the concordance among differential AF measures across pairs of polysomal and total RNA biological replicates, performing paired statistics (**Figure S1**). This approach identified 40 putative tranSNPs (**Figure 1A**), of which 21 located in 3'UTRs (**Table S2**).

Overall, we extended the methodology previously developed (Valentini et al. 2021) and observed that in HCT116, about 11% of genes with analyzable heterozygous SNPs show a difference in AF between paired total and polysome-bound mRNAs, suggesting allele-specific post-transcriptional and translational control.

Figure 1

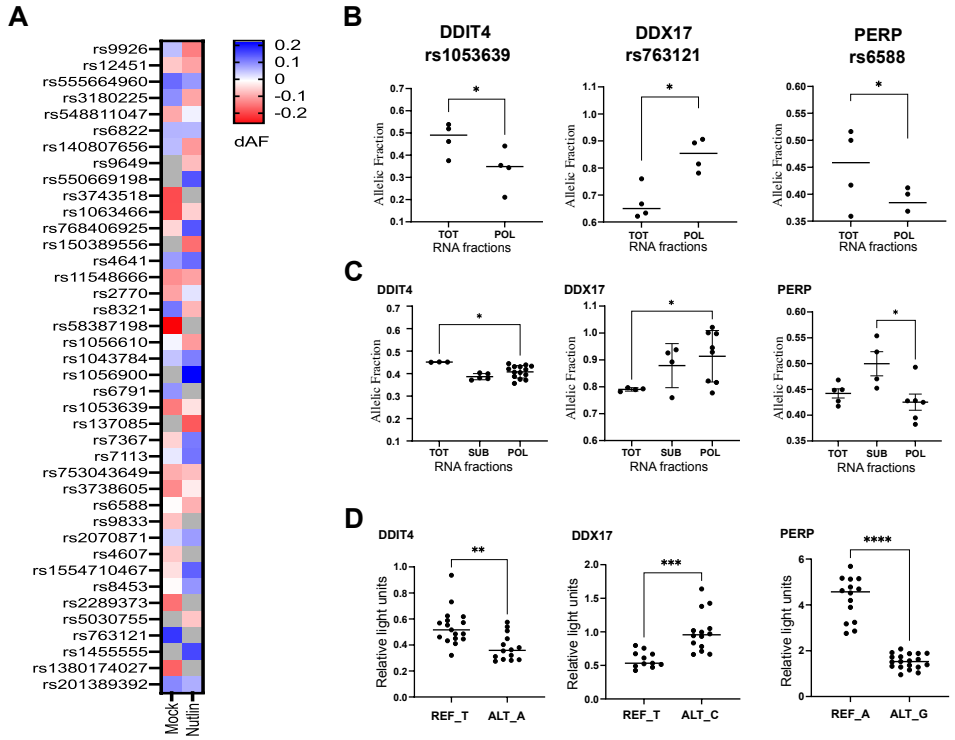


**Figure 1. The tranSNPs in the DDIT4, DDX17, and PERP genes are validated by orthogonal approaches.** A) Heatmap view of average differences in allelic fractions (AF) in the comparison between polysome-associated and total RNA for the 40 tranSNPs identified from the RNA-seq data from either mock or Nutlin-treatment conditions (Table S1 and S2 present the AF value for each biological replicate; accession number for the RNA-seq data: GSE95024). AF was computed as the number of reads for the alternative allele over the sum of reads of alternative and reference alleles. **B**) Plots of the AF for the rs1053639 -in DDIT4-, rs763121 -in DDX17-, and rs6588 -in PERP- tranSNPs obtained through RNA-seq of cytoplasmic total (TOT) and polysome bound mRNAs (POL). Individual replicates and the AF mean are plotted. *p-value < 0.05, two-tailed, paired t-test. **C)** AF values of the selected tranSNPs calculated from Sanger sequencing electropherograms, comprising also the sub-polysomal -RNP to 80S- (SUB) fractions. Individual replicates and the AF mean are plotted. *p-value < 0.05, two-tailed, paired t-test. **D)** Results of the dual luciferase assays presenting the relative activity (average and individual biological replicates) for the reference (REF_) and alternative (ALT_) alleles for each of the three selected tranSNPs cloned separately into the pGL4.13 vector immediately downstream the Firefly luciferase stop codon. Data was normalized using Renilla luciferase. **p-value < 0.01. ***p-value < 0.0005. ****p-Value < 0.0001, two-tailed, unpaired t-test.

Candidate tranSNPs for downstream analyses and validation were chosen considering several SNP statistics (**Figure 1B**, **Table S1**, **S2**) and information about the associated gene. Higher priority was given to SNPs with relatively high minor allele frequency (MAF), positioned in 3' UTR of genes whose expression is altered in cancer or whose function is associated with cancer-relevant

features, especially p53-related. We selected a total of four SNPs for validation (**Figure 1B-D, S1**). First, we sought to confirm differential allele-specific expression found in polysomes versus total RNA. Sucrose gradient density sedimentation of cytoplasmic lysates was performed (Pringle et al. 2019), and fractions were collected and analyzed by UV absorbance. RNA was recovered from the combined polysomal fractions and fractions corresponding to ribosomal subunits and 80S monosomes. Total RNA was also extracted. Amplicons were generated using primers specific for sequences surrounding the chosen SNPs (**Table S4**), Sanger sequenced, and the electropherograms were analyzed, expressing the results as AF (alternative allele signal over the sum of alternative + reference allele signals), as done for the RNA-seq data. For three out of the four chosen SNPs, an imbalance consistent in direction with what was measured in the RNA-seq dataset was found (**Figure 1C, S1D, S1F**). We also used an Ampliseq-based approach to measure allelic fractions from total and polysome-associated mRNAs obtaining results consistent with the RNA-seq and Sanger sequencing (**Figure S1G**). Next, we asked whether the candidate tranSNPs could exhibit allele-specific differences in activity when extracted from their native context. To this aim, we cloned ~500 nt fragments of the 3'UTR sequences harboring those SNPs downstream of a luciferase plasmid reporter, using HCT116 genomic DNA. Given the heterozygous state of the cell line, we retrieved clones for both alleles for each SNP. Dual luciferase assays were then performed in HCT116 cells, with results further supporting the observation that the SNPs and their immediate surroundings are sufficient to show allele-specific differences in reporter activity (**Figure 1C, S1**).

**Editing of HCT116 cells to obtain the three genotypes of rs1053639 tranSNP**

It is worth noting that while the heterozygous state and the comparison of AF among two RNA compartments (total versus polysomal) is necessary to enable reliable identification of tranSNPs in our approach, we expect that the homozygous state for alternative and reference alleles would reveal the highest level of phenotypic impact of this category of genetic variants. Hence, our next step was constructing potentially isogenic cell clones by CRISPR/Cas9-mediated editing. We exploited the CRISPR/Cas9-mediated knock-in delivering the Cas9 and the guide RNA (gRNA) as a ribonucleoparticle (RNP) to reduce its off-target potential (Ghetti et al. 2021). We first screened the gene sequences of the three validated tranSNPs candidate for the presence of the Protospacer Adjacent Motif (PAM) close to the tranSNP sites to explore the possibility of editing (**Figure S2A)**. Then, we designed a single gRNA (**Table S5**) in a position as close as possible to the tranSNP site to cut both alleles and maximize the efficiency of Homology-directed Repair (HDR). Based on the collective RNA-seq, validation data, editing amenability, and the relevance of the gene in cancer, including its functional links with p53 (Coronel et al. 2022; Schupp et al. 2013; Ellisen et al. 2002), the T/A rs1053639 in DDIT4 was a promising tranSNP. We delivered RNPs without donor DNA to test for cutting efficiency, as measured by TIDE (Brinkman and van Steensel 2019) (**Table S5**). The

rs1053639 gRNA presented a cutting efficiency of around 80%. We thus performed the knock-in and measured HDR efficiency by the ICE Synthego analysis web tool (Conant et al. 2022), which ranged from 5% to 9% for the initial bulk populations. With a single-cell cloning efficiency of about 1 to 3, 85 clones were isolated and characterized by Sanger sequencing. Collectively we obtained at least four clones homozygous for the rs1053639 T allele and four homozygous for the A allele. However, three clones (#3 TT, #5, and #6 AA) contained the same GGT 3 nt deletion, starting three nucleotides after the SNP site. We also obtained two clones bearing either a 9-nucleotide deletion (#7) or a 29-nucleotide deletion (#8) encompassing the SNP position (**Table S6**, **Figure S2B,** and methods). We considered at least two clones among the rs1053639 TT (#2, #3, #12, #13), and AA (#5, #6, #7, #10) along with the unedited AT clone (#1) to overcome the potential influence of clonal selection and adaptation and the above-mentioned editing limitations. We then used these cell models to study the SNP effect on various phenotypic assays.

**Higher DDIT4 protein levels in rs1053639 TT homozygous clones**

First, we tested the impact of the tranSNP status on DDIT4 steady-state protein levels (**Figure 2A, B**). TT clones exhibited significantly higher relative protein expression compared to AA clones, with the AT cells intermediate. This result was consistent with the change in AF from RNA-seq or Sanger sequencing that showed lower A allele representation in the polysomal fraction. The difference in protein levels was not dependent on changes in protein half-life (**Figure 2C**), nor on mRNA levels and turn-over (**Figure 2D**). An antisense DDIT4-AS1 transcript corresponding to the 3'UTR region was reported to affect the stability of the DDIT4 transcript (Yang et al. 2022; Fang et al. 2023). However, DDIT4-AS1 was equally expressed across TT and AA clones, and its expression was significantly lower than that of the DDIT4 transcript (**Figure 2E**). Next, we challenged the cells with Thapsigargin (100nM for 4 hours) (Kimball and Jefferson 2012; Protiva et al. 2008), an ER stressor (Sagara et al. 1992) that is a strong inducer of DDIT4 expression (**Figure 2F**). As expected, the treatment led to the marked induction of DDIT4 protein levels (**Figure 2G, 2H**). Notably, the difference in expression associated with the SNP genotype was maintained, and the lower expression of DDIT4 in AA clones was even more apparent. DDIT4 is also a recognized transcriptional target of p53, directly or through the transcription factor RFX7 (Ellisen et al. 2002; Coronel et al. 2022). Hence, we examined whether the rs1053639 alleles differed in DDIT4 expression also in response to p53 activation. Results showed that while the MDM2 inhibitor Nutlin led to comparable induction of p53 protein across the HCT116 DDIT4 clones, the associated induction in DDIT4 protein was higher for the TT homozygous clones and intermediate for the AT cells (**Figure S3A-S3C**). AA clones did not show significant DDIT4 induction in response to Nutlin.

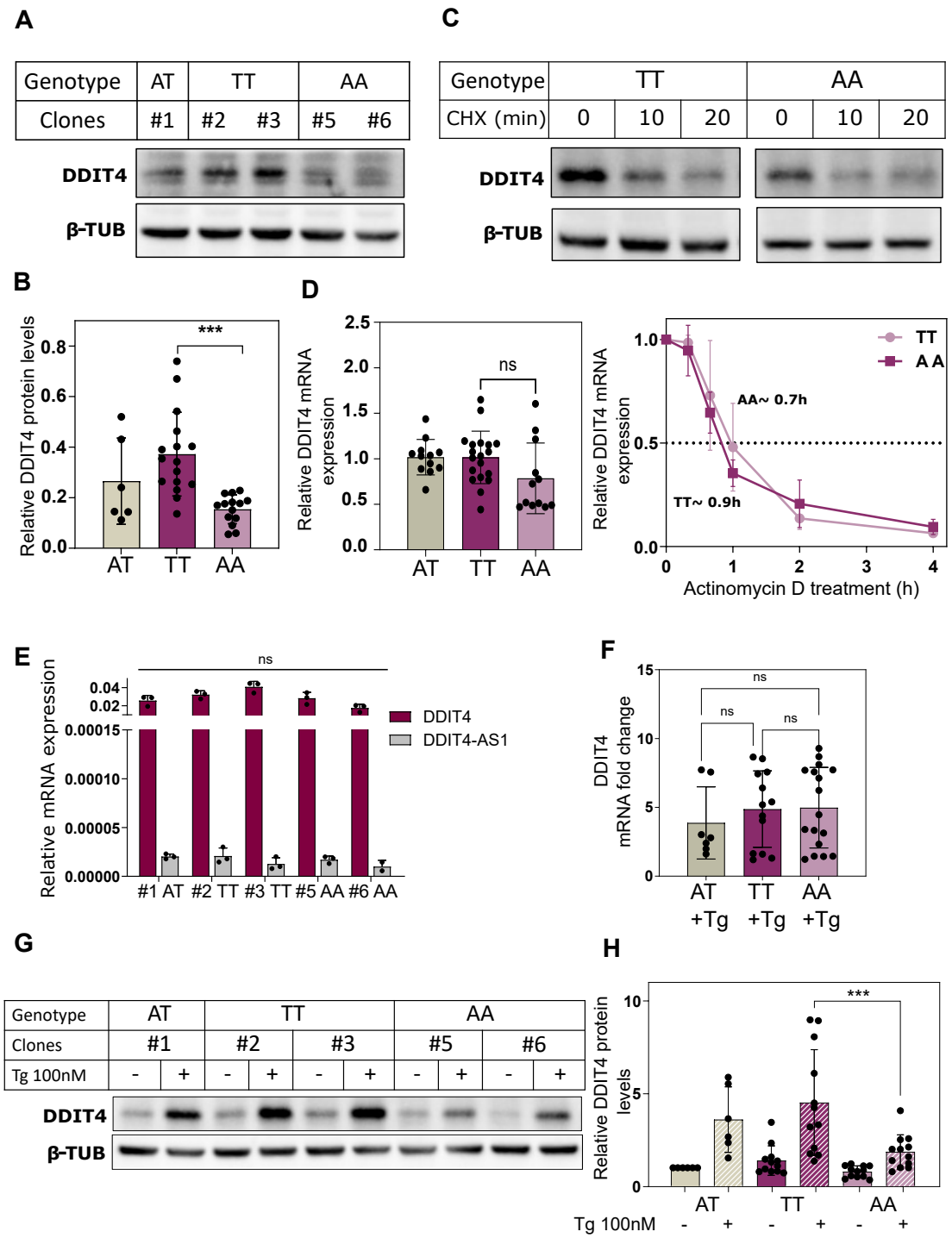


**Figure 2. rs1053639 tranSNP impacts DDIT4 protein expression in HCT116-derived cell trios.**
HCT116 cells were edited by CRISPR/Cas9 RNPs and donor DNA to obtain cell trios with the three genotypes for the rs1053639 tranSNP located in the proximal portion of the DDIT4 3'UTR. **A)** Western blot analysis of DDIT4 protein expression in HCT116 cells (A/T heterozygous) and DDIT4 rs1053639 homozygous clones (TT, AA). β-Tubulin was used as a reference. **B)** Densitometry analysis of the blots from several biological replicates shows a significant difference in relative DDIT4 protein abundance with the different tranSNPs genotypes. ***P-value <0.005 Ordinary one-way ANOVA. **C)** Western blot analysis of DDIT4 protein in HCT116 TT and AA homozygous clones for the rs1053639 treated with 100µg/ml cycloheximide (CHX) at the indicated time points. β-Tubulin was used as a reference. **D)** (Left) Relative DDIT4 mRNA expression as measured by RT-qPCR and normalized to GAPDH and YWHAZ. Student's t-test shows no significant differences in DDIT4 mRNA expression in the different clones. ns, not significant. (Right) Estimation of DDIT4 mRNA stability following inhibition of transcription by actinomycin D treatment (10µg/ml). The curve presents the residual relative DDIT4 mRNA levels (average and standard deviation of at least three biological replicates) at various treatment time points measured by RT-qPCR decay from HCT116 clones harboring TT or AA genotypes. The estimated half-lives of the DDIT4 mRNA in TT and AA homozygous clones are indicated. **E)** DDIT4-AS1 and DDIT4 mRNA levels measured by RT-qPCR

and normalized to GAPDH across TT and AA clones. The expression of DDIT4-AS1 was neglectable compared to the expression of the sense DDIT4 mRNA in our cellular models. Data represents the mean ± SD of three independent experiments. ns, not significant. **F)** HCT116 clones were exposed to 100nM thapsigargin (Tg) or vehicle for 4 hours, and the induction of DDIT4 mRNA was measured by RT-qPCR with clones of the three rs1053639 genotypes. Average, standard deviation, and individual replicates are presented. ns, not significant, student's t-test. **G-H**) Western blot and densitometry analysis showing relative DDIT4 protein induction upon thapsigargin (Tg 100nM) treatment of the three rs1053639 genotypes. β-Tubulin served as a control. ***p-value <0.005, unpaired t-test.

Since we observed higher polysomal association and higher DDIT4 protein levels from the rs1053639 T over the A allele we examined at higher resolution the relative DDIT4 mRNA distribution across the sucrose gradient. For this experiment, RNA was recovered from ten individual fractions along the polysome profile (fractions 3 to 12, **Figure S4A**), and the DDIT4 mRNA distribution, along with CDKN1A and RPS26 controls, was measured by qPCR. Results were plotted as relative abundance, as previously described (Panda et al. 2017). In the mock condition, AA cells showed a slight reduction in translation efficiency for the DDIT4 mRNA, as revealed by higher relative abundance in lighter polysomes (fraction 9) (**Figure 3A**).

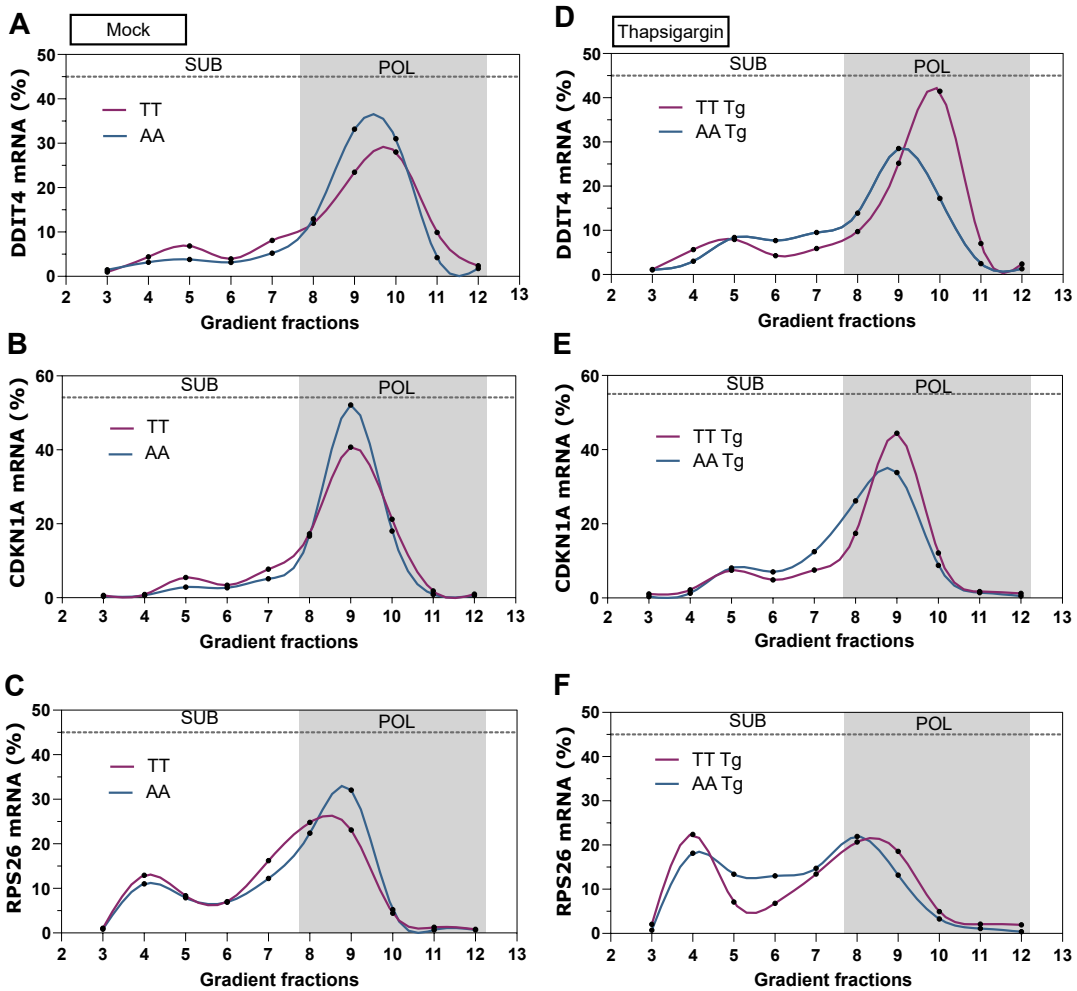


**Figure 3. DDIT4 rs1053639 impacts its own mRNA distribution in polysomes.**
Cytoplasmic lysates from HCT116 rs1053639 homozygous (TT, AA) clones treated with thapsigargin 100nM or vehicle for four hours, were subjected to fractionation through sucrose density gradients (15 to 50%). Polysome profiles are shown in Figure S4A. **A-D)** The distribution of DDIT4 mRNA (Mock, thapsigargin) across the 12 gradient fractions was quantitatively analyzed across the two genotypes by RT-qPCR. Relative mRNA % in every fraction was plotted. Three

independent biological experiments were performed. CDKN1 **B-E)** and RPS26 **C-F)** mRNAs were used as control transcripts and were analyzed using the same methodology as described for DDIT4 mRNA.

No differences were instead apparent for CDKN1A and RPS26 mRNAs, which, in fact, showed a trend for slightly higher abundance in fraction 9 in AA cells (**Figure 3B, 3C**). When the same analysis was performed after Thapsigargin treatment, the difference became particularly visible for the DDIT4 mRNA, with the mRNA distribution peaking in fraction ten in TT but in fraction nine for AA cells (**Figure 3D-F**). Collectively, the results are consistent with the lower relative translation of the A allele originally identified from the AF value from the RNA-seq dataset (in heterozygous cells, **Table S2**). We concluded that tranSNP rs1053639 alleles are associated with differences in DDIT4 protein expression both in basal and inducing perturbations.

**The rs1053639 tranSNP genotype impacts DDIT4 mRNA fate through the RBMX protein**

We developed predictions for allele-specific binding starting from a list of 552 RNA binding proteins (RBPs) with consensus binding motifs (Cook et al. 2011), using the TESS software (DOI:10.1002 /0471250953.bi0206s21) (Schug 2008) (**Table S3**). The predictions pointed to RBMX, ACO1, and YBX1 as RBPs which might differentially bind to the T/A alleles. Recent PAR-CLIP data in HEK293T cells (Liu et al. 2017) highlighted that RBMX binds in the 3'UTR of DDIT4 mRNA, therefore, we decided to focus on this target RBP. RBMX is mainly nuclear located, can interact with structural features of mRNAs, and was reported to modulate mRNA splicing, processing, and degradation (Heinrich et al. 2009; Zuccotti et al. 2020; Liu et al. 2023b; Dassi et al. 2013). Hence, we performed RNA electromobility shift assays using the full-length recombinant RBMX protein and RNA probes mimicking the secondary structure of T and the A alleles of the endogenous DDIT4 mRNA. For the RNA probe design, we took advantage of three learning-based methods (EternaFold, CONTRAfold, and Ufold), two thermodynamic-based methods (ViennaRNA and RNAstructure), and one hybrid method (MXFold2) (Sato et al. 2021; Fu et al. 2022; Lorenz et al. 2011; Wayment-Steele et al. 2022). Although the global structure of the 3'UTR was not significantly impacted, significant differences in the local secondary structure were observed after changing the base at the SNP site. RNA EMSA revealed that both RNA probes are bound by RBMX *in vitro*, with a possible preference for the T allele (**Figure 4A**). We further explored the publicly available web service AlphaFold 3 to generate accurate structure predictions for protein-RNA interactions. Interestingly, AlphaFold 3 provided several models confirming that the T allele RNA EMSA probe is located in a more favorable spatial conformation than the A allele probe for RBMX binding (**Figure S5A**). It also predicts that the C-terminal low complexity domain of RBMX binds to DDIT4 mRNA. We then performed RIP assays to evaluate this interaction in a cellular context. The antibody used proved to be effective for the RIP protocol (**Figure S5B**). We first performed RIP in parental HCT116 cells, followed by Sanger sequencing of the input and IP samples. However, we could not appreciate quantitative differences in RBMX binding across the two alleles with this assay (**Figure S5C**). We

next used both the rs1053639 TT and AA clones to perform RIP-qPCR. The qPCR analysis revealed that RBMX binds to DDIT4 mRNA slightly less than the positive control CSDE1, and we could confirm the preferential binding to the rs1053639 T allele (**Figure 4B**).

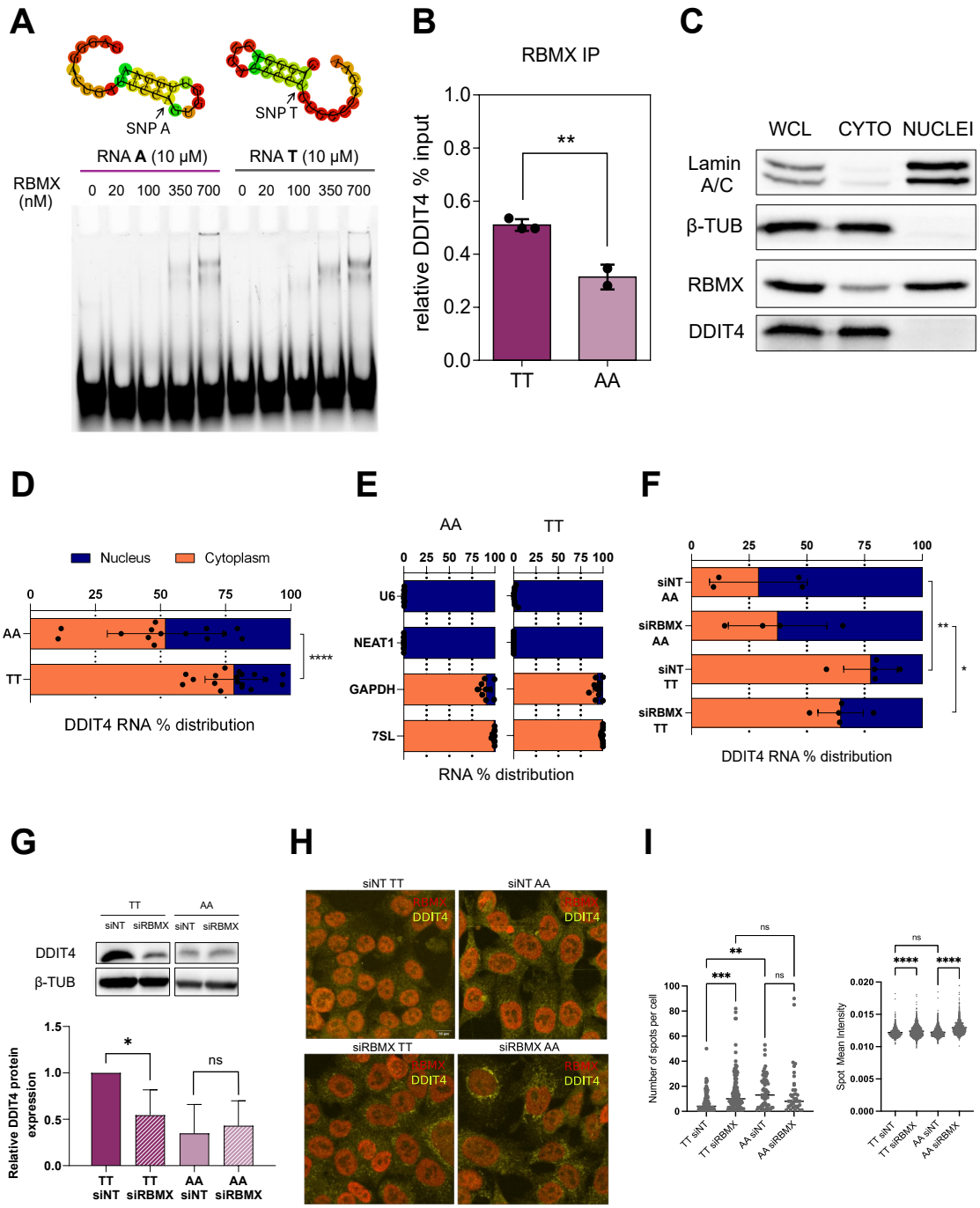


**Figure 4. The rs1053639 tranSNP genotype impacts mRNA fate through the RBMX protein.**
**A)** Structural RNA probes were designed based on RNA folding prediction tools. RNA EMSA was performed using the full-length recombinant RBMX protein and the above-mentioned RNA probes. In the '0' lane, the RNA probe was incubated with the binding buffer and the protein elution buffer. RNA-protein complexes were resolved on a native 6% gel. **B)** The endogenous RBMX protein was immunoprecipitated from a whole cell lysate in TT and AA clones. Results are expressed as the percentage of the target DDIT4 mRNA relative to the input sample and normalized to the positive control CSDE1 mRNA to account for the variability in RIP efficiency. At least two independent biological replicates were performed. **C)** Cell fractionation was performed in HCT116 cells and protein levels were evaluated. Lamin A/C (70-75 kDa) was used as a marker of the nuclear fraction, and β-Tubulin (55 kDa) was used as a marker of the cytoplasmic fraction.

DDIT4 protein was found exclusively in the cytoplasm. RBMX is mostly a nuclear protein as previously reported. WCL: whole cell lysate. CYTO: cytoplasm. **D)** RNA levels were evaluated in TT and AA cells upon cell fractionation followed by RT-qPCR. The distribution of DDIT4 mRNA is significantly different among TT and AA cells, with DDIT4 mRNA from TT cells being considerably more enriched in the cytoplasm. Data represent the mean ± SD of at least four independent experiments. The relative expression of the gene in the cytoplasm is calculated as the fold change of the Ct in the cytoplasm compared to the Ct in the nucleus, with nuclear and cytoplasmic RNAs eluted in the same volume of water. ****p-value < 0.0001. Unpaired t-test. **E)** U6 snRNA and NEAT1 were used as markers of the nuclear fraction, 7SL and GAPDH were used as markers of the cytoplasmic fraction. However, GAPDH mRNA is not absolutely cytoplasmatic, consistent with previous reports. Markers for the AA cells are shown on the *left*, and markers for the TT cells are shown on the *right*. **F)** RBMX was knocked down in TT and AA cells. DDIT4 mRNA levels in control (siNT) and knocked-down samples (siRBMX) were evaluated in TT and AA cells upon cell fractionation followed by RT-qPCR. Upon RBMX silencing, the intracellular distribution of DDIT4 mRNAs was slightly mitigated. Data represent the mean ± SD of three independent experiments. *p-value 0.0114 **p-value 0.0031, unpaired t-test. **G)** DDIT4 protein levels in control (siNT) and knocked-down samples (siRBMX) were evaluated in TT and AA cells upon cell fractionation followed by western blot. Representative blot of DDIT4 protein levels across TT and AA clones (Top). Densitometry analysis of the blots from several biological replicates shows that DDIT4 protein levels in TT clones decrease to the levels of the AA clones upon RBMX knock-down. *p-value < 0.05. Unpaired t-test. **H)** Confocal images of smiFISH-IF of cell clone #3 (TT) and clone #6 (AA) after control (siNT) or RBMX silencing for 72 hours. RBMX protein is shown in red, DDIT4 mRNA is in yellow. Scale bar is 10 µm. I) At least three fields (15-20 cells per field) for each coverslip and each condition were imaged, and cytoplasmic spots were quantified using Cell-Profiler 4.0.7 (Broad Institute, Inc.) and segmenting them as objects with a typical diameter range of 10 to 30 pixels. (Left panel), number of DDIT4 mRNA spots per cell. (Right panel), spot mean intensity. ** p< 0.01; *** p<0.001; **** p<0.0001, ordinary one-way ANOVA. ns = not significant.

Given the nuclear localization of RBMX and its binding to DDIT4 mRNA, we decided to examine the relative subcellular localization of DDIT4 mRNA alleles. Specifically, nuclear and cytoplasmic fractions were obtained and verified both at protein (**Figure 4C**) and RNA levels (**Figure 4D, 4E**). Results indicate that the DDIT4 mRNA shows higher cytoplasmic localization in the TT clones while being significantly more nuclear in the AA ones. To shed light on the contribution of RBMX to this phenotype, we confirmed that our edited cells expressed it at comparable levels, and we used siRNAs to deplete its expression by ~50% (**Figure S5D, S5E**). Fractions upon RBMX silencing were verified at the RNA level (**Figure S5F**). RBMX silencing led to a slight increase of nuclear DDIT4 mRNAs in TT clones (**Figure 4F**), and, importantly, to a significant decrease of DDIT4 protein levels (**Figure 4G**). Single-molecule FISH showed a punctuated distribution of the DDIT4 mRNA, particularly in the perinuclear region of the cytoplasm. The number of granules per cell was higher in the AA compared with the TT clones. Interestingly, the depletion of RBMX led to a significant increase in granularity in TT cells that reached the levels observed in the AA ones (**Figure 4H- J**). Hence, we suggest that RBMX contributes to the rs1053639 allele-specific regulation of DDIT4 protein levels through multiple mechanisms that include export, cytoplasmic localization, and translatability of the DDIT4 mRNA.

**The rs1053639 tranSNP genotype impacts on mTOR pathway markers**

Since DDIT4 is an established inhibitor of mTORC1, (Brugarolas et al. 2004; Deyoung et al. 2008; Coronel et al. 2022) we next sought to investigate whether the effect of rs1053639 on DDIT4 protein levels would impact features of the mTOR pathway as well. In particular, we analyzed the levels of EIF4EBP1 and S6K phosphorylation both in basal culture conditions and in response to Thapsigargin treatment. We observed unexpectedly higher levels of relative phospho-eIF4EBP1 and phospho-S6K

for TT clones in basal conditions, suggesting that our clones may have acquired compensatory mechanisms to balance their metabolism (**Figure 5A-D**) (Leprivier and Rotblat 2020; Sengupta et al. 2010). Instead, in response to Thapsigargin treatment, TT clones were associated with a significant reduction in those mTORC1-dependent phosphorylations, which was not changed in the AA clones. Analysis of the protein levels of the ER stress response markers ATF4, a transcription factor regulating DDIT4 expression (Whitney et al. 2009; Han et al. 2021) (**Figure 5E**), and of the transcript levels of CHOP, spliced XBP1, and SESN2 (**Figure 5F**) did not reveal differences among HCT116 clones with the three rs1053639 genotypes in response to Thapsigargin (**Figure 5G**).

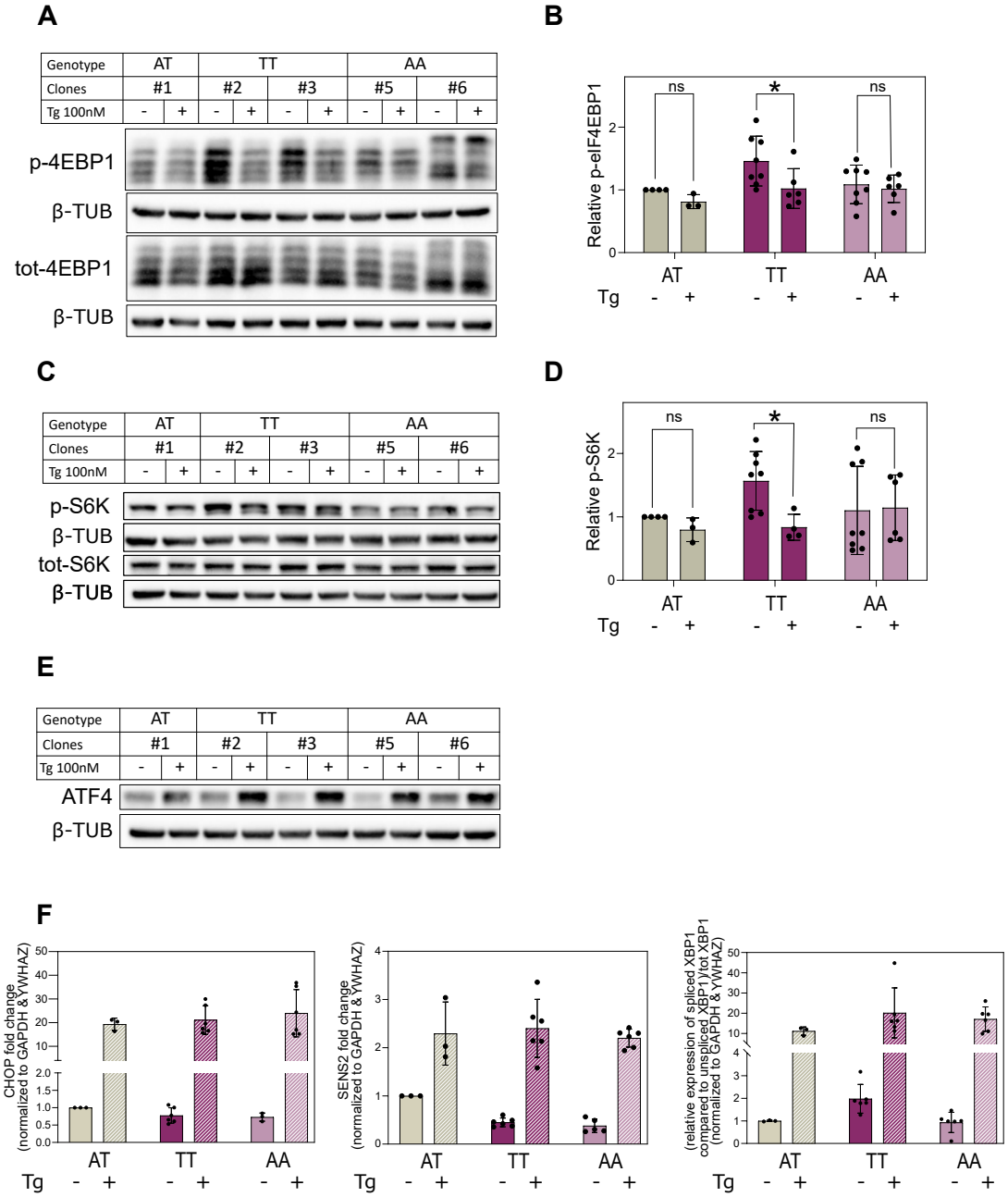


**Figure 5. DDIT4 rs1053639 genotype-specific effect on the mTOR pathway.**
HCT116 parental cells and clones differing for the rs1053639 homozygous genotypes were treated with either thapsigargin 100nM or vehicle control for 4 hours. **A, C)** Cell lysates were analyzed by immunoblotting for the phosphorylation state and levels of the mTORC1 target eIF4EBP1 and S6K proteins. **B, D)** Densitometry analysis of all blots reveals that significant inhibition of the phosphorylation of both eIF4EBP1 and S6K proteins is apparent only in the rs1053639 TT homozygous clones. *p-value <0.05. ns, not significant. **(E, F)** Markers of the ER stress response are activated in HCT116

cells in response to thapsigargin treatment independently from the rs1053639 genotype. **E)** Western blot analysis of ATF4 protein induction upon thapsigargin (Tg 100nM) treatment in HCT116 cells (A/T heterozygous) and DDIT4 rs1053639 homozygous clones (TT, AA). β-Tubulin was used as a reference. **F)** Relative CHOP, SENS2, and spliced XBP1/ un-spliced XBP1 mRNA expression as measured by RT-qPCR and normalized to GAPDH and YWHAZ.

We concluded that the rs1053639 SNP status does not broadly impact the activation of the ER-stress response upstream of DDIT4. Consistent with the effect of Thapsigargin treatment, a more pronounced reduction in phospho-eIF4EBP1 was observed for TT homozygous cells also in response to Nutlin treatment (**Figure S3A, D**).

Next, we investigated if the differences in the mTOR pathway led to changes in global translation or proliferation of the HCT116 edited clones. The global translation was monitored either in mock culture conditions or in response to Thapsigargin treatment using a quantitative analysis of the Translation Efficiency (TE) measured as the relative abundance of polysomes compared to the 80S from polysomal profiling or the measurement of newly synthesized peptides using either a commercially available global protein synthesis kit or a puromycilation assay (**Figure 6A-C**, **Figure S4A**).

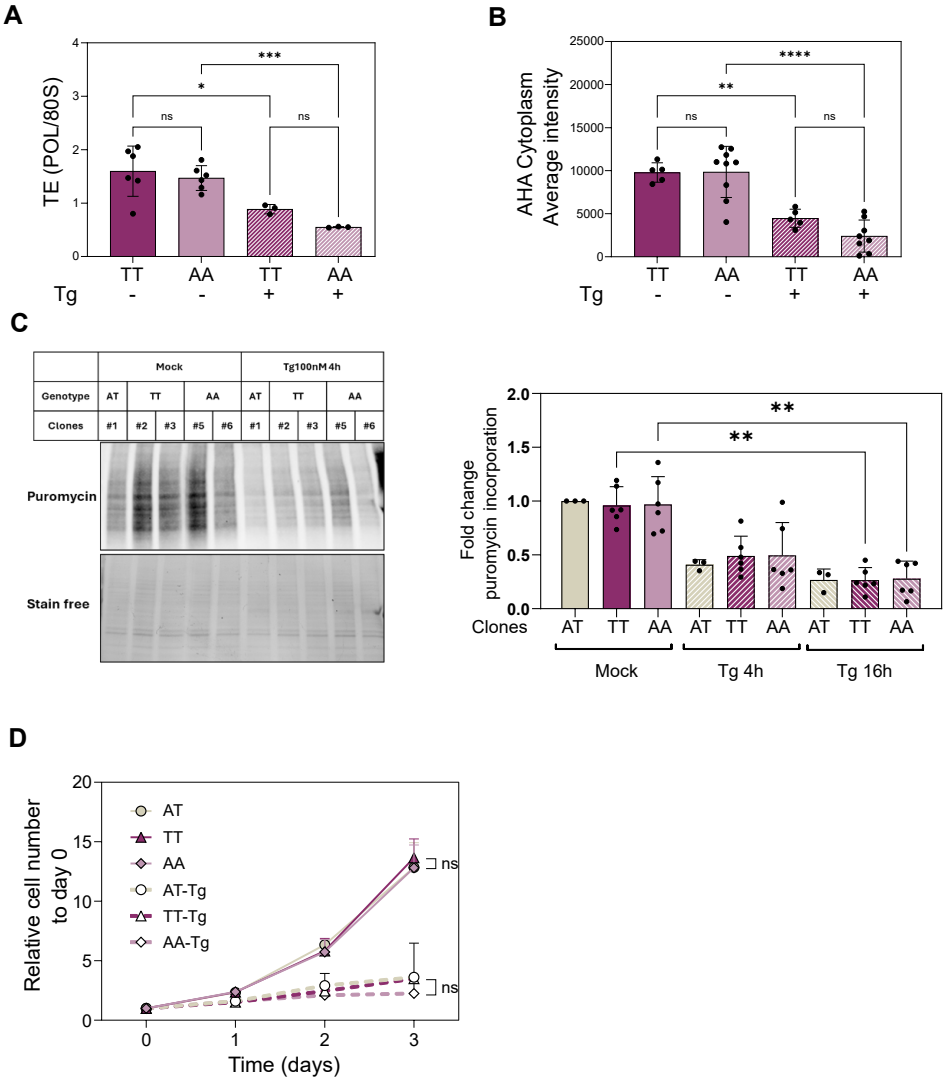


**Figure 6. The DDIT4 rs1053639 genotype does not significantly impact global translation and cell proliferation in response to Thapsigargin.**

**A)** Global Translation Efficiency (TE) measured from polysome profiles (see Figure S4) prepared using sucrose gradient fractionation of homozygous TT and AA HCT116 cells treated as in Figure 1A. **B)** Global translation measured by a Click-it reaction assay after incubation of the cells with a modified methionine for 30 minutes. Homozygous TT and AA HCT116 cells grown in mock condition or treated with 100nM Thapsigargin for four hours were tested. In both assays, Thapsigargin led to a reduction in global translation. **C)** Global translation measured by a puromycilation assay. A representative Western blot is presented on the left: immunodetection with an antibody targeting puromycin and the loading control is shown. The bar graph on the right plots the results of the densitometric analysis of the blots plotted as fold change of puromycin incorporation for the indicated HCT116 clones and treatment conditions. Average, standard deviations and individual replicates are shown. *P-value < 0.05; **P-value < 0.001; ***P-value < 0.0005. **** P-value < 0.0001, two-tailed, unpaired t-test. **D)** HCT116 cells parental and clones differing for the rs1053639 homozygous genotypes were treated with thapsigargin 10nM of vehicle control for 72 hours. The proliferation of the clones was followed every 24 hours by the Operetta HCS system. Relative cell number curves were plotted as the mean of several replicates ± standard deviation (SD). ns, not significant. Ordinary two-way ANOVA.

In all cases, there were no significant differences in global translation comparing TT and AA rs1053639 clones, although the latter showed a trend for a stronger reduction in the perturbed conditions. The relative proliferation of the clones was similar in the mock condition as well as in response to Thapsigargin (**Figure 6D**), while TT clones showed slightly higher resistance to Nutlin treatment (**Figure S4B**). We concluded that the rs1053639 tranSNP genotype did not show an overt difference in global translation or cell proliferation.

**The rs1053639 tranSNP AA genotype shows a competitive growth advantage in prolonged culture conditions.**

Given the contribution of DDIT4 in the negative modulation of a critical and intricate metabolic hub such as mTOR (Dennis et al. 2014), we tried to tease out possible differences in cellular phenotypes due to the rs1053639 genotypes through co-culture experiments where cells could experience fluctuations in nutrient availability in the media. To visualize and count the contribution of each genotype to the total co-culture population, derivative GFP or RFP positive clones were obtained with high clonal purity. Cells were seeded in 6-well plates, and relative cell number was measured either at Operetta High Content Screening (HCS) or by FACS, examining the population every four days, up to fifteen days. Results were expressed as relative fitness, as recently described (DIas Louro et al. 2024) (**Figure 7A**). Interestingly, while the rs1053639 TT cells showed higher fitness at early times, AA cells progressively gained a proliferative advantage. This result was not influenced by the presence or the type of fluorescent marker (**Figure S6A**). To further explore this significant difference related to rs1053639, cells were sorted seven days after co-culture, and the two rs1053639 genotypes were examined separately. No significant difference in cell cycle distribution was observed (**Figure 7B**). Finally, the co-culture experiment was repeated in the presence of the Q-VD-OPh pan-caspase inhibitor (Keoni and Brown 2015). The progressive advantage of the AA genotype was confirmed, suggesting that apoptosis was not involved in this phenotype (**Figure 7C**). Doxorubicin 3μM was included as a control to induce apoptosis (Wang et al. 2004; Hamadou et al. 2021) (**Figure S6B**).

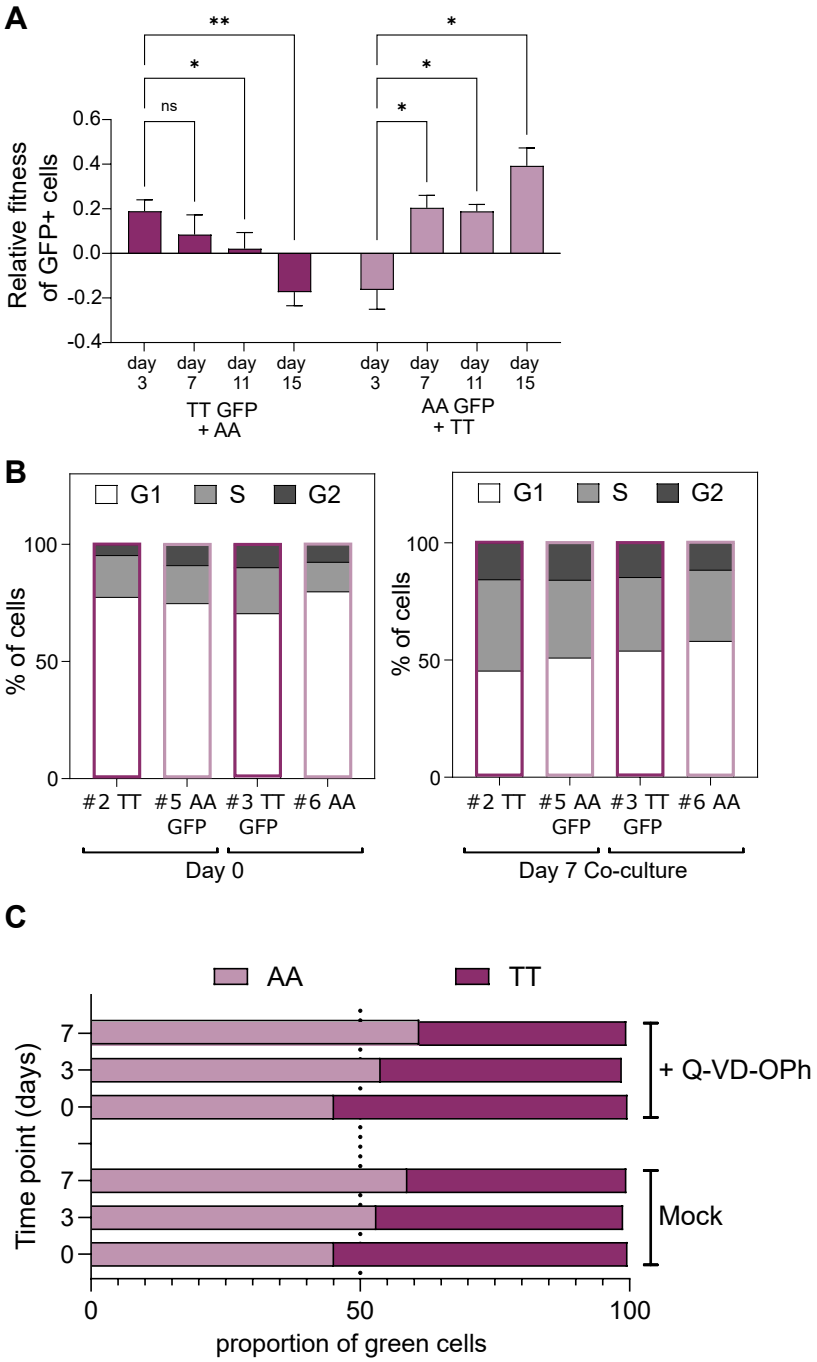


**Figure 7. DDIT4 rs1053639 impacts cellular dynamics and survival under stress and competitive conditions**

**A)** DDIT4 clones harboring the TT genotype were transduced with Lentiviral particles to constitutively express EGFP. After transduction, cells were treated with 5 µg/ml blasticidin for at least 15 days, to reach at least 95% of GFP+ cell populations. DDIT4 clones harboring the AA genotype (not fluorescent) were mixed ~1:1 with EGFP-expressing TT genotype cells and co-cultured over 15 days. The relative growth was assessed by flow cytometry analyzing 10K cells. Cellular fitness of the GFP+ clones relative to GFP- competitor clones was calculated as follows: pGFP+(t) = NGFP+(t) / (NGFP+(t) + N GFP-(t)), W = ln ((pGFP+(ti) /pGFP-(ti) ) / (pGFP+(t0) /pGFP-(t0)), adapting a described method (DIas Louro et al. 2024) . The error bars represent the mean ± SD of at least eight independent experiments (Four TT GFP+, four AA GFP+). **P-value <0.005. *P-value < 0.05 Ordinary two-way ANOVA. **B)** Cell cycle analysis by flow cytometry (FACS) for single clones before co-culture (Left) and sorted clones seven days after co-culture (Right). **C)** TT and AA clones were co-cultured as described in A) for seven days, treated with the pan-caspase inhibitor Q-VD-OPh 10µM or vehicle control, and analyzed by FACS at day 0, 3, and 7. The graph represents the proportion of GFP+ cells across time points and conditions. Doxorubicin 3µM was used as a positive control to induce apoptosis (Figure S6B).

**The rs1053639 tranSNP AA genotype showed faster growth and a competitive advantage when xenografted in Zebrafish embryos.**

The proliferation experiments in co-culture suggested to us that the rs1053639 tranSNP genotype could impact cell growth in challenging environments where nutrient concentrations vary, and different cell types can compete. To explore this hypothesis and also gain some information on the potential aggressiveness of our edited cancer cell lines, we developed xenograft experiments in Casper Zebrafish embryos (White et al. 2008), following a published protocol adjusted for our experiments (Marines et al. 2023). Equal number of cells of the two different genotypes labeled either with GFP or RFP as described earlier, were injected into the swim bladder of three-day post-fertilization embryos. Cells were then imaged the following day and again 48 hours later. Results, plotted as a percentage of tumor cells' growth comparing 24 to 72 hours post-injection, showed that, when cells of the two genotypes were pre-co-cultured *in vitro* for three days prior to injection in the embryos, the growth advantage of the AA genotype was again apparent (**Figure 8A, B**, **S7A**).

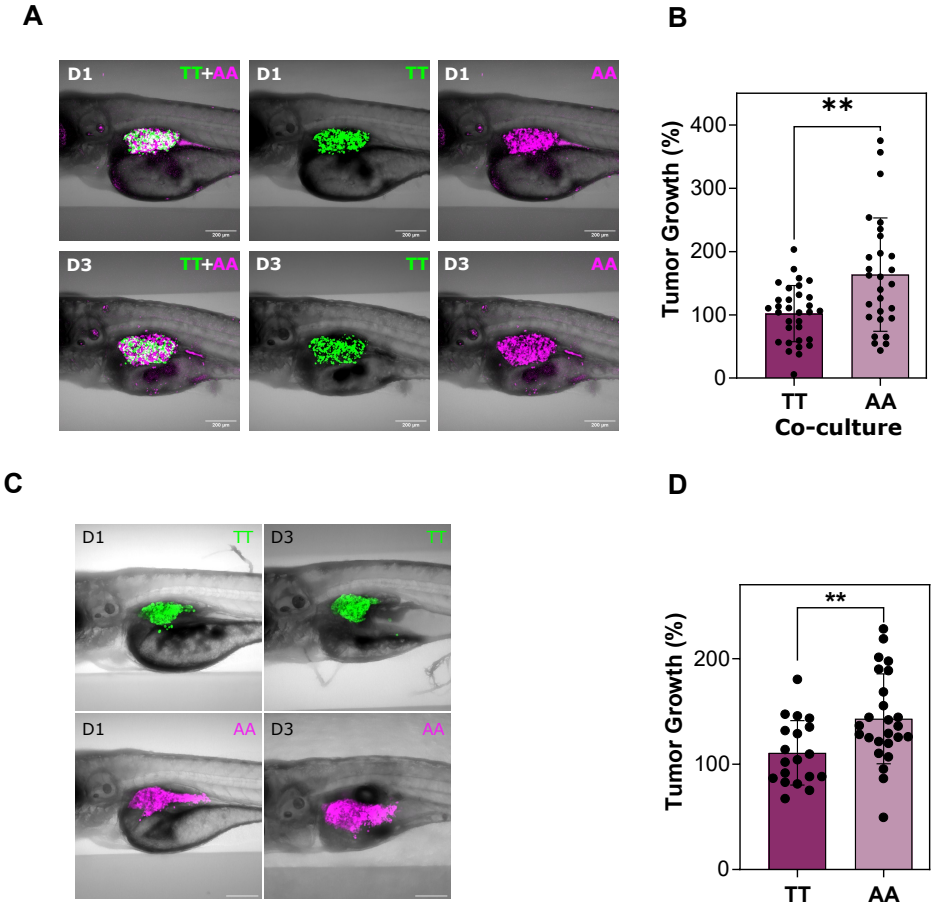


**Figure 8. DDIT4 rs1053639 impacts tumor growth and genotypic competition in zebrafish larvae xenotransplants.** DDIT4 rs1053639 homozygous clones, transduced with lentiviral particles to constitutively express either EGFP or MiRFP as described in Figure 5A, were xenotransplanted into zebrafish larvae two days post-fertilization. Tumor growth was monitored over a three-day period, with a minimum of 30 larvae per genotype condition. Representative confocal microscopy images were captured on day 1 and day 3 post-transplantation, with TT clones shown in green and AA in purple. **A)** DDIT4 clones expressing GFP (TT clones) were mixed~ 1:1 with RFP-expressing clones (AA genotype) and were initially co-cultured *in vitro* for four days, followed by xenotransplantation into ~30 zebrafish larvae for an additional three days of *in vivo* co-growth prior to confocal imaging. **B)** Bar graph illustrating the percentage of tumor growth relative to day 0 of transplantation, with each data point representing an individual larva. AA clones harbor significantly higher fitness. **P-value < 0.005. paired t-test. **C)** TT and AA clones were separately xeno-transplanted into zebrafish larvae,

which were followed for three days and imaged by confocal microscopy. **D)** Quantitative analysis of tumor growth indicates a significantly faster growth rate for AA than TT cells *in vivo*. Each data dot represents one larva. **P-value < 0.005. paired t-test.

Furthermore, we evaluated the proliferative potential of the TT and AA cells separately in the *in vivo* setting. Notably, the AA cells grew more compared to the TT ones as well (**Figure 8C, D, S7B**). Collectively, co-culture experiments indicate that rs1053639 AA cells display a competitive advantage over TT cells both *in vivo* and *in vitro*, although the underlying mechanisms remain to be clarified, and it does not seem to fit under a classical cell competition response (Bowling et al. 2018).

**The rs1053639 tranSNP status can have prognostic significance in cancer patients.**

The phenotypic differences related to the rs1053639 genotype, a relatively common SNP in the human population, led us to explore whether this tranSNP status can impact clinically relevant variables in cancer patients. Based on the results obtained with the trio of genotypes, and in particular the reduced control of the mTOR pathway of the AA homozygous cells, we decided to focus on a recessive model, comparing AA homozygous patients with AT plus TT. Using TCGA data we observed worse prognosis for AA patients in both colorectal and esophageal cancers (**Figure S8A, S8B**). DDIT4 mRNA expression showed a prognostic value with high expression, which is associated with reduced survival probability in lung adenocarcinoma but higher survival probability in esophageal cancers, according to recent reports (Song et al. 2021; Fattahi et al. 2021; Chen et al. 2023). In colon adenocarcinomas, DDIT4 mRNA expression is significantly higher compared to healthy tissues (p-value $8.9e^{-21}$) (**Table S8**). Further, data in DepMap indicate a reasonable level of correlation between DDIT4 protein and mRNA levels (Pearson 0.517, linregress p-value $8.82e^{-5}$) (**Figure S8C**). We began exploring the correlation between rs1053639 genotype and DDIT4 protein levels by IHC in seven biopsies of primary colorectal adenocarcinoma and adjacent resected normal tissues. To this aim, DNA from peripheral blood was obtained from the same group of samples, and the DDIT4 SNP status was genotyped (**Figure S8D**). The samples were classified by certified pathologists in two categories based on IHC intensity. The average signal intensity on the different samples, first classified as Low, Intermediate, and High, was re-evaluated using Fiji, and it was found that the average intensity of the Intermediate samples was comparable to the average intensity of the Low samples. Therefore, it was decided to reduce the classes from three to two (Low and High). Overall, cytoplasmic expression of DDIT4 protein was higher in the cancer samples than in healthy tissue from the same patient. Only one sample (TT) received a high score both for normal and tumor sections (**Figure S8D**, **E1**, and **E2**). Further studies are needed to establish the value of rs1053639 SNP status as a prognostic marker.

## Discussion

*Variation in allelic imbalance in polysomal RNA as a tool to identify functionally relevant SNPs.*

Our approach to identifying tranSNPs is based on computing and comparing relative changes in allele counts across mRNA fractions, building upon the methodology introduced in (Valentini et al. 2021). By fully leveraging biological replicates, our enhanced method eliminates the need for a predefined threshold to detect allele-specific expression. Instead, it evaluates differential allelic fractions between RNA-seq data from the two distinct cellular compartments using pairwise statistics, thereby improving the robustness of the analysis. Despite the limitations imposed by low coverage, which introduced noise in allelic fraction estimates and constrained our ability to detect and characterize SNPs with significant allelic imbalances, our findings support the presence of signal in over 11.5% of analyzable genes. Each of these genes harbors one or multiple imbalanced SNPs, collectively accounting for approximately 7% of all analyzable SNPs—aligning with previous reports (Valentini et al. 2021; Przytycki and Singh 2020).

One underlying assumption in our approach is that the interaction of an mRNA with polysomes is directly proportional to the amount of protein being produced. While this is a generally accepted feature in translatome studies (Wang et al. 2020), approaches differ in how polysome-associated RNA is isolated. In our study, we used linear gradients to separate ribosomal subunits, 80S, and polysomes (2 or more ribosomes). In a more restrictive approach, non-linear sucrose gradients were optimized to collect only the mRNAs associated with three or more ribosomes (Gandin et al. 2014; Liang et al. 2018). This latter approach could reveal more instances of allele-specific translation efficiency, resulting in only a shift in the relative abundance within light and heavy polysomes. This is, in fact, appreciable also in our fraction-by-fraction qPCR study for the DDIT4 mRNA (**Figure 7**).

*Mechanism of rs1053639 impact on DDIT4 protein expression.*

For rs1053639 A/T we observed a significant reduction in the alternative allele (A) in polysome-associated mRNAs in the mock condition. Validation of allelic imbalance by Sanger sequencing was performed with independent biological replicates of polysome profiles, and we examined total RNA, ribosomal subunits, and polysomes separately. We also observed consistent results using an Ampliseq-based targeted resequencing. We then examined, using the edited HCT116 clones homozygous for the alternative and reference alleles, respectively, the relative distribution of the DDIT4 transcript along the polysome profile after having established that in mock conditions, there were no overt changes in global translation. While the results indicated a higher proportion of the A allele with lighter polysomes, the magnitude of the difference indicated that translation efficiency per se does not seem to fully explain the marked difference in DDIT4 protein expression associated with the different SNP status. In our analysis pipeline, we also used predictions of trans factors binding to mRNAs. In this respect, rs1053639 is predicted to affect an RBMX binding motif. Considering that

RBMX (hn-RNPG) binding to mRNAs can be influenced directly or indirectly (through structured motifs) by m6A (Liu et al. 2017) and that a recent study, pointed to an important role of m6A in DDIT4 mRNA half-life (Qin et al. 2021), we assessed SRAMP predictions of methylatable sites (Zhou et al. 2016). While the tranSNP position is not an m6A methylation site, there is a predicted very high confidence m6A site located 9 nucleotides upstream. The same region was identified by miCLIP in HeLa cells (Yang et al. 2019). We attempted to perform GLORI-seq on TT and AA cells, however, the extremely GC-rich region surrounding the SNP didn't allow us to quantify m6A levels at the site of interest using this technology (Liu et al. 2023a) (data not shown). Nevertheless, we cannot exclude a role for m6A in guiding the effector functions of RBMX in our model as well or in guiding the allele-specific binding of RBMX since m6A has been reported to locally alter the RNA structure to favor the binding of RBMX (Liu et al. 2017). Hence, local structural changes in the RNA structure generated by the tranSNP may cooperate with m6A-switch mechanisms to eventually control the accessibility of the RBMX binding site in an allele-specific manner.

Given that RBMX is reported as prevalently nuclear (Heinrich et al. 2009), an observation confirmed also for HCT116 cells (**Figure 4C**), we measured DDIT4 mRNA localization comparing the TT and AA homozygous clones. Results indicated higher cytoplasmic localization for the T allele. The transient silencing of RBMX slightly increased the nuclear localization of the T allele and significantly increased the number of perinuclear granules of DDIT4 mRNA. This effect was associated with a significant reduction of DDIT4 protein expression with the TT genotype, making it comparable to the levels of the AA clones. In cells of the AA genotype, the number of DDIT4 mRNA perinuclear granules was lower than in TT cells in the mock condition. Interestingly, RBMX depletion did not significantly change the nuclear localization of the DDIT4 mRNA A allele, the number of perinuclear granules per cell, or DDIT4 protein levels.

Collectively, our validation experiments confirmed the observation of allelic imbalance in polysomes and provided evidence that rs1053639 can impact DDIT4 protein expression through a mechanism that comprises mRNA localization, modification, and translation efficiency.

*Implications of rs1053639 allelic status on DDIT4-mediated functions*

DDIT4 is an established important negative modulator of the mTOR pathway, acting at the level of mTORC1. Consistently, its gene expression is modulated in response to ER stress, with ATF4 as an important transcription factor. It is also inducible by hypoxia and is considered a p53 target gene, although recent data proposed that the contribution of p53 is indirect, via the transcription factor RFX7 (Coronel et al. 2022). In general, mTOR inhibition is growing in relevance in p53-dependent tumor suppression (Kon et al. 2021). The negative modulation of mTORC1 by DDIT4 is rather established, although reports differ on the exact mechanism (Dennis et al. 2014; Deyoung et al. 2008) and its relative relevance in different cell types (Chen et al. 2016). DDIT4, as the extended name testifies, is considered a player in the DNA damage response, although also, in this regard,

mechanistic details are missing. Overall, DDIT4 function in cancer is considered to be tumor suppressive. For example, a relatively recent screen indicated DDIT4 in a short list of p53 pathway targets with strong tumor suppressive potential. In agreement with the centrality of the mTOR pathway for general cell metabolism, DDIT4 has emerged as an important gene in contexts other than cancer, such as liver disease, neurodegeneration, pulmonary injury, and retinopathy (Rittenhouse et al. 2013; Qin et al. 2021; Malagelada et al. 2006; Yoshida et al. 2010). In fact, post-transcriptional regulation of DDIT4 expression has been the subject of different studies that can bear relevance for understanding the impact of rs1053639. For example, two studies pointed to the important role of an antisense transcript (DDIT4-AS1) corresponding to a large portion of DDIT4 3'UTR and of the 3' coding sequence, although with different conclusions on the role of the antisense transcript on the sense one (Yang et al. 2022; Fang et al. 2023). rs1053639 is included in the antisense. A splicing event that enables the design of antisense-specific primers. We checked if the allelic status could somehow impact the amount of spliced DDIT4-AS1. In HCT116, the antisense was expressed at a very low level, and there were no appreciable differences among the edited clones (**Figure 2**), indicating that it does not contribute to the difference in DDIT4 protein expression in our context.

In HCT116 cells, our experiments demonstrate that rs1053639 SNP status significantly impacts DDIT4 protein levels. The lower expression of DDIT4 in AA homozygous clones is even more pronounced when the gene transcription is induced by ER stress or by Nutlin. Hence, the tranSNP we identified is predicted to impact p53-dependent and, more in general, stress-dependent modulation of DDIT4 with potentially appreciable consequences on the negative modulation of mTOR, impacting translation control, proliferation, autophagy, and cell survival. Given the complex regulation of the mTOR pathway (Goul et al. 2023), the impact of DDIT4 is expected to be at least in part influenced by tissue type. In HCT116 cells, higher DDIT4 protein levels in the TT homozygous clones are associated with stronger repression of mTORC1 markers. Despite this, TT and AA clones showed similar proliferation in culture plates. However, in vitro co-culture experiments showed a higher proliferation of AA cells. We attempted to measure markers of mTOR pathways after sorting AA and TT cells from the cocultures, but the quantities of recovered proteins did not enable us to reach conclusive results (data not shown). The two separated populations did not show evidence of cell cycle checkpoint activation or apoptosis induction. We suggest that AA cells, by having a reduced control relaxed negative inhibition of mTORC1 through DDIT4, could fare better under conditions of transient nutrient deprivation. The results of the xenograft transplantation experiments in Zebrafish embryos were also consistent with higher proliferation of HCT116 cells homozygous for the rs1053639 A allele.

In general terms, DDIT4 is considered a tumor suppressor gene. However, gene expression data from TCGA indicate an almost equal number of cancer types where DDIT4 expression is higher in normal tissues than in cancer compared to the opposite trend. Also, in terms of survival analysis, high DDIT4 expression has been associated either with a better or worse prognosis. Although the data is

exploratory in nature, we found consistent prognostic predictions when TCGA patients' cohorts were stratified based on DDIT4 mRNA levels or for the rs1053639 genotype for LUAD, ESCA, and COAD.

*Study Limitations*

The limited coverage of our RNA-seq dataset resulted in a relatively small number of heterozygous SNPs available for analysis. This was further constrained by our conservative approach, which requires the heterozygous state of an mRNA variant, a minimum of twenty reads, and consistency among four biological replicates of total and polysomal RNA sequencing that are then compared to nominate a tranSNP candidate. This strategy reduces the number of genetic variants that can be analyzed with a chosen cell line but enhances the likelihood of detecting true signals. Validation experiments using orthogonal approaches and reporter assays were limited to four selected candidates of which three showed consistent results across methods. While the heterozygous state is a requirement to start our analysis, the phenotypic impact of a variant is expected to be most pronounced in homozygous states. Therefore, confirming the causal role of a tranSNP on cell phenotypes requires the development of genomically edited, isogenic cell clones differing for SNP status, a time-intensive process that, in our study, was performed only in HCT116 cells.

*Conclusions*

We have developed a robust pipeline to catalog genetic variants associated with allele-specific changes in mRNA translation leveraging biallelic mRNAs and polysomal profiling as a proxy for translation efficiency (**Figure 9**). Using this approach, we identified 40 SNPs that exhibit allelic imbalance when comparing total and polysomal RNA. Focusing on rs1053639 in the DDIT4 3'UTR we found that the alternative (A) allele is associated with reduced DDIT4 protein levels in the human colon adenocarcinoma-derived HCT116 cells. This reduction correlates with a higher abundance of the A allele in the nucleus and an increased number of DDIT4 perinuclear cytoplasmic mRNA granules. These allele-specific differences are mediated by the RNA-binding protein RBMX. Cells homozygous for the alternative A allele exhibit lower DDIT4 protein levels, leading to diminished negative regulation of the mTORC1 pathway, enhanced growth potential in zebrafish xenografts, and poorer prognosis in selected TCGA cancer cohorts. More broadly, our approach provides a powerful framework for identifying genetic drivers of inter-individual variability in mRNA translation, shedding light on mechanisms that can influence cancer progression.

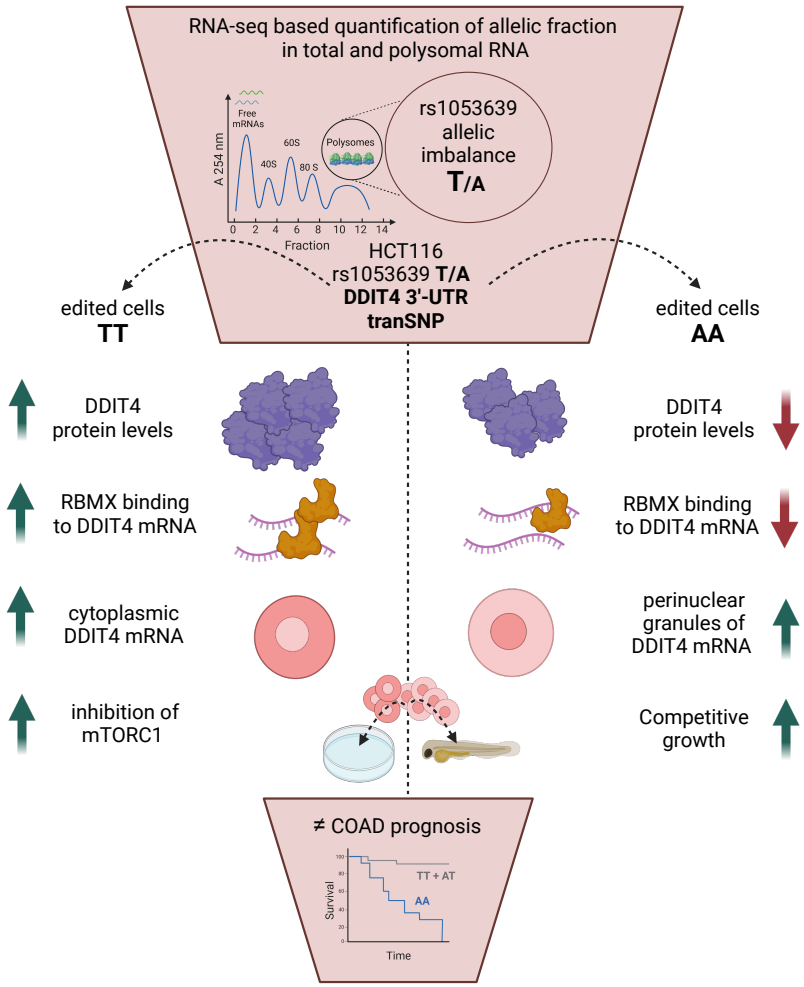


**Figure 9. Graphical Summary** Scheme of the approach taken to identify tranSNPs and of the results obtained with rs1053639 in DDIT4 with the HCT116 cell model.

**Acknowledgments**
We thank Dr. Ainan Geng and Prof. Hashim M. Al-Hashimi, Department of Biochemistry and Molecular Biophysics, Columbia University, NYC, USA, for the DDIT4 3'UTR RNA structural predictions. We thank Dr. Mounira Chalabi, Ribosome, Translation and Cancer Team Universite' Claude Bernard Lyon, France, for technical support to M.H.H. We thank Alice Casata, Irene Cagol, Massimo Andreis, Micol Bottamedi, Federica Sontacchi and Christian Cestaro for technical support during their Bachelor's internships. We thank Dr. Ezequiel Mariano Rivero and prof. Fatima Gebauer, Gene Regulation, Stem Cells, and Cancer Program, Centre for Genomic Regulation (CRG), Barcelona, Spain, for support with RIP protocol.

**Funding**
This work was supported by Fondazione AIRC under the grant IG #25849 "Mining common genetic variants impacting on allele-specific translation and cancer risk" to A.I, the European Union under NextGenerationEU, PNRR M4C2 INV 1.1, PRIN 2022 PNRR Prot. n. P2022A9J9L to L.L.F. L.A. was supported by an AIRC short-term fellowship. M.C.M. and F.L. were supported by AIRC IG 2021 no. 25704. A.L. and M.H.H. were also supported by Short-term scientific mission fellowships by the "Translation Control in Cancer" European Network", Translacore Cost Initiative (CA21154). This work was also partially supported by the initiative "*Dipartimenti di Eccellenza* 2023-2027 (Legge 232/2016)" funded by the MUR, and by FESR 2023 – "Sostegno alle Infrastrutture di Ricerca".

## Materials and methods

### Cell lines and cell culturing
The human cell line HCT116 was purchased from the Biological Resource Center ICLC Cell bank. Cells were cultured in standard Roswell Park Memorial Institute (RPMI) 1640 medium (GIBCO) supplemented with 10% fetal bovine serum (FBS), 100 units/ml penicillin, 100 mg/ml streptomycin antibiotic mix (GIBCO), and 2 mM Glutamine (GIBCO). The cells were maintained in a humidified atmosphere at 37°C and 5% $CO_2$.

### Dataset and data preprocessing
The RNA-sequencing data of RNA extracted from polled polysomal and total cytoplasmic fractions of HCT116 cells cultured either in mock condition or treated with the MDM2 inhibitor Nutlin was produced in our earlier study (Rizzotto et al. 2020). The raw data is deposited in GEO, under the GSE95024 accession number. Single-end RNA-seq data was processed to obtain from row FASTQ files properly processed BAM files. The trimming step, essential to remove sequence adapters, was performed with Trimmomatic (Bolger et al. 2014). The data were aligned with STAR (Dobin et al. 2013) to the reference genome GRCh38 to obtain a BAM file for each sample. To improve the characterization of SNP positions, a step of deduplication to remove PCR artifacts was performed by employing PICARD module MarkDuplicates (broadinstitute.github.io/picard/). Then, GATK (Depristo et al. 2011) was employed to split, realign, and recalibrate the data in order to improve the quality of the alignment. The pileup of SNPs positions was performed with ASEQ (Romanel et al. 2015) using parameters mode=0, mbq=20, and mrq=20 in order to obtain allelic fraction (AF) calculations. Only SNPs in exonic and UTR regions extracted from dbSNP were considered. We emphasize that, as expected, the use of single-end RNA-seq data led to high duplication rates (on average 70%), limiting the number of SNPs we could characterize and analyze. Nevertheless, this step, along with subsequent quality control processes, was essential to ensuring high-quality AF estimations.

.

**Differential ASE analysis**

The allelic fraction at SNPs' positions was used to compute differential allele-specific expression (ASE) events between total and polysomal RNA fractions. In order to capture those events, we started by identifying all SNPs that were heterozygous in at least one biological replicate of the two fractions. More specifically, for the data obtained both in mock and nutlin-treatment conditions, we searched for SNPs having a value of AF between 0.2 and 0.8 (i.e., heterozygous genotype) in at least one replicate of one of the two fractions (polysomal or total) and that was confidently observable (i.e., depth of coverage of at least 20x) in the corresponding fraction. A total of 1060 SNP/condition pairs were identified. Of these, only those with AF measures available across all four biological replicates and both fractions were then considered for differential ASE analysis (N=582, Table S1).

To assess the presence of a differential ASE event at a SNP position we extended the methodology we developed (Valentini et al. 2021). In particular, for each SNP we exploited the concordance of differential AF measures across pairs of polysomal and total RNA biological replicates by performing paired t-test statistics. Although none of the 41 SNP/condition pairs with nominal p-value $\leq 0.05$ kept significance after FDR correction, likely due to the low coverage that increased the noise in AF estimations, overall, 11.8% of the analyzed genes had one or multiple SNPs (in LD) with a p-value $\leq 0.05$, strongly supporting the presence of a true signal. A list of SNPs with nominal p-values $\leq 0.05$, denoted as putative tranSNPs, were hence retained for downstream analysis and experimental validation.

**Expression analysis of DDIT4 in cancer and normal tissue samples**

To test whether the gene containing the rs1053639 tranSNP exhibits differential expression in tumor versus normal tissue samples, we compared transcript expression values (normalized RPKM values) of the DDIT4 gene exploiting primary tumor and normal tissue samples from the TCGA COAD dataset. In detail, we downloaded the gene counts for all genes from the recount 3 database (Wilks et al. 2021), and RPKM values were computed using the function *getRPKM* from the recount 2 R package. Then, protein-coding transcripts were selected, and their RPKM values were normalized across samples using the R limma quantile normalization function. Then, focusing on the DDIT4 gene, the distributions of log2(RPKM+1) values across tumor and normal samples were compared using Wilcoxon's test statistics, and p-values were finally corrected for multiple hypotheses using the FDR method.

**Survival assay using TCGA data**

Genotype and survival data for TCGA patients were collected. Specifically, genotype information for rs1053639 tranSNPs was retrieved from (Valentini et al. 2022), while survival data across different endpoints (Overall Survival, Disease-Specific Survival, Disease-Free Interval, and Progression-Free Interval) was retrieved from (Liu et al. 2018). A recessive model (AA+AB vs. BB) was built, and for each endpoint, a Kaplan-Meier survival curve was calculated along with summary statistics obtained from a multivariate Cox proportional hazards regression model, where age at diagnosis was included as a covariate. For each endpoint, the analysis was performed across 23 different cancer types, and p-values were corrected for multiple hypothesis testing, retaining only associations with a p-value $< 0.05$ and an FDR $< 0.25$. Survival analyses were performed using the survival R package.

**Identification of SNPs disrupting putative RBP consensus motifs**

To investigate the RNA protein binding landscape at the rs1053639 tranSNPs locus, we retrieved 552 human RNA binding consensus motifs from the RBPDB database (Cook et al. 2011) and created a

FASTA file containing a list of 60bp DNA sequences containing the reference and the alternative bases. Then, TESS software (Schug 2008) was run to compute RBP consensus motifs scores. A set of log-likelihood-ratio-based scores were computed: the log-odds ratio of the match for the alternative and reference bases (*altScore* and *refScore*), and the maximum possible log-odds ratio for a match for a given RBP consensus motif (*maxScore*). The scores were filtered by keeping only the forward strand analysis. Results were retained only if the score for the reference or the alternative allele was at least 3 and greater than 0.5 when normalized by the *maxScore*.

**Polysome profiling, RNA extraction, and Sanger sequencing**

HCT116 cells were grown in 150 mm dishes to 80% confluence followed by 100 nM Thapsigargin or vehicle treatment for 4 hours. Cells were then incubated for 10 min with 50 µg /ml cycloheximide at 37°C to disrupt the protein synthesis process and halt translation elongation, thereby immobilizing the ribosomes on the mRNAs and preventing ribosome disassembly. Cells were rinsed with ice-cold PBS containing 50 µg /ml cycloheximide and then gently scraped using 600 µl of ice-cold lysis buffer (20 mM Tris-HCl pH 7.5, 100 mM KCl, 5 mM $MgCl_2$, 0.5 % Nonidet P-40, 0.2 U/µl RNasin® Ribonuclease Inhibitor [Promega], cOmplete™, Mini Protease Inhibitor Cocktail 1X [Roche], 100 µg /ml cycloheximide) and collected in an Eppendorf tube. The cells were then incubated on ice for 10 min and centrifuged for 10 min at 12,000 *x g* at 4 °C to remove the nuclei. The cytoplasmic lysate was then separated by ultracentrifugation in a Beckman SW41 rotor at 40.000 rpm for 1 hour and 40 minutes at 4°C after being loaded onto a 15-50% linear sucrose gradient dissolved in salt buffer (100 mM NaCl, 20 mM Tris-HCl pH7.5, and 5 mM MgCl2). The sucrose gradients were fractionated, and the absorbance was measured at 254 nm by the Teledyne Isco model 160 gradient analyzer equipped with a UA-6 UV/VIS detector. Based on density separation, polysomes were isolated from the fractions, and RNA was harvested from these polysomes with the TRIzol® reagent (Invitrogen ™) following the manufacturer's protocol. The RNA was then retro-transcribed, and the sequences containing the candidate TranSNPs were amplified by PCR using AmpliTaq Gold 360 Master Mix (ThermoFisher Scientific) and specific primers (**Table S4**). The PCR products were purified by the spinNAker GEL&PCR DNA purification kit (Euroclone) and subjected to Sanger sequencing by Mix2Seq Kit (Eurofins Genomics) following the manufacturer's protocol. Total RNA was also harvested in parallel for Sanger sequencing. Analysis of the electropherograms was performed by Fiji software. Quantification was performed by assessing the area under the peaks of the tranSNP nucleotides as a metric to calculate allelic fraction. The normalization process considered the relative efficiency of the four nucleotides' incorporation during sequencing, using the information of local surroundings. The allelic fraction for targeted genes was determined for at least three independent experiments. Student's t-test was used to calculate the p-value.

**Targeted RNA sequencing by Ampliseq**

Quality control of raw reads was performed using FastQC (https://www.bioinformatics.babraham.ac.uk/projects/fastqc/). Adapter trimming and quality filtering were then conducting with Trimmomatic v0.39 (Bolger et al. 2014) and CutAdapt 4.1 (Martin 2011) to remove Nextera adapters and primer sequences. The resulting FASTQ files were then aligned to the GRCh38 reference genome using STAR v2.7.10b (Dobin et al. 2013), and alignment files were further processed with clipOverlap tool implemented into BamUtil software v1.0.15 (https://genome.sph.umich.edu/wiki/BamUtil:_clipOverlap) to trim overlaps between paired reads. Pileup files and variant statistics, including coverage supporting the reference allele, coverage supporting the alternative allele, and the variant allelic fraction, were generated using PacBAM (Valentini et al. 2019).

**TranSNP 3'UTR cloning**

The 3'UTR regions surrounding the candidate TranSNPs were amplified from the HCT116 genomic DNA, using primers containing XbaI and EcoRI restriction sites and resulting in ~500 bp fragments. (**Table S4**). The resulting PCR fragments were cloned immediately downstream of a modified Firefly Luciferase in pGL4.13 [Luc2/SV40] vector (Promega), where a linker sequence adding an EcoR I site (F: 5' cAa**gaattc**atatgcccgggt 3', R: 5' ctagacccgggcatat**gaatt** 3') was inserted at the original Xba I site to facilitate the insertion of fragments in a desired orientation. Correct cloning was confirmed by colony PCR and Sanger sequencing.

**Plasmid DNA transfection and Luciferase assay**

HCT116 cells were seeded into 96-well plates and transiently transfected the empty pGL4.13 modified plasmid or those containing the allele-specific 3'UTRs fragments along with the Renilla control luciferase (pRL-SV40) in A 3:1 ratio (60 ng plus 20 ng) using Lipofectamine™ LTX and Plus™ Reagent (ThermoFisher Scientific). After 48 hours, Firefly and Renilla luciferase activities were quantified using a Dual-Luciferase™ Reporter (DLR™) Assay System (Promega).

The transfected cells were lysed with 50ul 1X Passive Lysis Buffer for 15 minutes. The lysates were resuspended, and 15ul of the resuspension was transferred to a white 384-well plate. Subsequently, 15ul of LAR (Luciferase assay reagent) was added, and the luminescence was read at the Varioskan LUX Microplate reader. Following this, 15ul of the Renilla substrate was added, and the Luminescence was measured again to quantify Renilla luciferase expression. RNA (TRIzol Reagent, Invitrogen) was extracted from the lysates, and the Firefly Luciferase mRNA was quantified by qPCR for additional normalization.

**CRISPR/Cas9-mediated knock-in**

Edited HCT116 clones at the SNP sites were generated exploiting a CRISPR-Cas9 mediated knock-in with the Cas9 delivered as a ribonucleoparticle (RNP), as previously described (Ghetti et al. 2021). The same protocol with few modifications (not providing the donor DNA as a template for repair and not inhibiting DNA-PKcs) was used beforehand to test the cutting efficiency of the guide RNA (gRNA). For both protocols, the gRNA was prepared by mixing 1:1 Alt-R® CRISPR-Cas9 crRNA (IDT™) and Alt-R® CRISPR-Cas9 tracrRNA (IDT™). The mixture was heated at 95°C for 5 minutes and let cool down at room temperature for 5 minutes for optimal annealing. 3 µl of gRNA were further incubated with 120 pmol of recombinant Cas9 for 20 minutes at room temperature to generate the ribonucleoprotein (RNP). In parallel, previously seeded HCT116 wild-type cells were harvested by trypsinization, and 2.5 x $10^5$ cells per condition were electroporated in the 4D-Nucleofector™ System (Lonza) using the SE Cell Line 4D-Nucleofector™ X Kit S (Lonza) as described in (Ghetti et al. 2021). The electroporation mixture combined 20 µl of cell suspension, 1.2 µl of Alt-R® Cas9 Electroporation Enhancer (IDT™), 5 µl of RNP complex, and PBS to a final volume of 30 µl. In addition to these, 1.2 µl of Ultramer® DNA Oligonucleotide (100 µM, IDT™) were added in the case of knock-in generation to provide a template donor DNA for HDR. Electroporated cells were recovered from the strip and seeded in a 12-well plate format either untreated or, in the case of knock-in generation, treated with 1 µM of NU7441 DNA-PKcs inhibitor for 48 hours to favor HDR occurrence. The media, both with and without the drug, was changed after 24 hours. The cells were kept in culture up to full recovery and expanded until 2.5 x $10^5$ cells could be harvested for DNA extraction and Sanger sequencing. DNA was extracted by adding 20 µl of the QuickExtract™ DNA Extraction Solution (Lucigen) to the cell pellet. After vortexing, the sample was incubated at 65°C for 15 minutes and 98°C for 10 minutes. 1 µl of this DNA was used for the PCR amplification using the GoTaq® Green Master Mix (Promega) in 25 µl of reaction. PCR primers (**Table S4**) were specifically designed to produce 300-700 bp long amplicons and to have the SNP of interest asymmetrically located 100-200 bp from one or the other end of the amplicon, to have

optimal sequencing interpretation. The PCR product was then purified using the MinElute™ PCR Purification Kit (QIAGEN). 75 ng of purified PCR products were sequenced using the Mix2Seq Kit and Sanger sequencing service provided by Eurofins. The TIDE software (Brinkman et al, 2014) was employed to identify and quantify insertions and deletions (indels) in the bulk edited population and infer cut efficiency percentages. On the other hand, the Synthego ICE software (Synthego Performance Analysis, ICE Analysis. 2019. v3.0) was employed to assess the knock-in efficiency in the edited bulk population. A limiting dilution assay was performed on the knock-in edited bulk population by seeding 1 cell/well in 96-well plate format to eventually obtain clones. The media was changed once a week for 3-4 weeks, then potential clones were expanded to 24-well plates, and at the same time, pellets were harvested for DNA extraction and sequencing. The efficiency of clone production was about 1 in 3 seeded cells. About 80 clones were screened by sequencing.

**cDNA synthesis and qRT-PCR**

RNA was extracted by using the TRIzol® reagent (Invitrogen™) or the NucleoSpin ® RNA kit (Machery-Nagel) based on the downstream applications. RNA purity and quantity were assessed by NanoDrop™ Spectrophotometer (Thermo Fisher Scientific), followed by random primer-mediated reverse transcription using the RevertAid First Strand cDNA Synthesis Kit (Thermo Fisher Scientific) with 1000 ng of RNA as input. The cDNA was diluted 1:8 and 12.5ng -total RNA equivalent- in 10µl reaction were used in the following RT-qPCR analysis with the qPCRBIO SyGreen Mix (PCR Biosystems). All reactions were performed in 384-well plates using the QuantStudio™ 5 Real-Time PCR System (Applied Biosystems®) instrument. Primers were designed using Primer Blast (NCBI) and are listed in **Table S4**. All kits were used following the manufacturer's instructions. All qPCR reactions were performed in triplicate, and Cq values were averaged. The fold change was calculated using *dCt* and normalized to at least two gene references.

**RNA half-life measurement**

3 x $10^5$ HCT116 cells from edited clones were seeded in a 6-well plate format. After 24 hours, cells from the first timepoint (t0) well were collected by trypsinization. The cell pellet was resuspended in 500 ul of TRIzol® reagent (Invitrogen™) and frozen at -80°C. The media was aspirated from the remaining wells and replaced with 10 ug/ml Actinomycin D in 2 ml of fresh media to achieve RNA polymerase II inhibition. After 20 minutes, 40 minutes, 1 hour, 2 hours and 4 hours from the treatment, cells were pelleted from the corresponding timepoint wells and resuspended in TRIzol®. Once all the pellets were recovered and frozen, they were thawed at room temperature for 15 minutes and RNA was extracted following the TRIzol® manufacturer's instructions. RNA was quantified using the NanoDrop™ Spectrophotometer (Thermo Scientific™) and 1000 ng of timepoint t0 RNA from each HCT116 clone was retro-transcribed using the RevertAid First Strand cDNA Synthesis Kit (Thermo Scientific™) with random hexamers. For timepoints > t0, RNA was retro-transcribed volumetrically to the reference t0 for each clone. The cDNAs were diluted 1:8 and 2 µl in 10 µl of reaction and were used in the following RT-qPCR analysis with the qPCRBIO SyGreen Mix (PCR Biosystems) and the QuantStudio™ 5 Real-Time PCR System (Applied Biosystems®) instrument. Primers are listed in **Table S4**. GAPDH and 18S rRNA levels were also evaluated as stable mRNAs. The mRNA abundance was calculated relative to the start of transcription inhibition (t0) for each HCT116 clone (2^-dCt). The mRNA decay rate was calculated by a nonlinear regression curve fitting using the one-phase decay function (GraphPad Prism version 10).

**Western blot analysis**

1.6 x $10^5$ HCT116 cells from edited clones were seeded in a 6-well plate format. When cells reached 70 - 80 % confluence, they were treated with 100 nM Thapsigargin or vehicle for 4 hours. Cells were washed with PBS, and total cellular protein was isolated using a RIPA buffer containing protease inhibitor cocktail (cOmplete™, Mini Protease Inhibitor Cocktail, Roche). Lysates prepared for analysis of phosphorylated proteins were supplemented by a phosphatase inhibitor cocktail (Phosphatase Inhibitor Cocktail I, MedChemExpress). After vortexing and incubation at 4°C for 20 min, cell lysates were centrifuged at 15000 rpm at 4°C for 15 min, with supernatant collected and stored at -80°C. Prior to western blotting, the lysates were denatured by boiling at 95°C for 10 min in 1x Laemmli Sample Buffer (Bio-Rad). The protein concentration in each sample was determined using Pierce™ BCA Protein Assay Kits (Thermo Fisher Scientific). Equal amounts of protein from each lysate were then subjected to SDS-PAGE and electrophoretically transferred to a nitrocellulose membrane (Cytiva Amersham™ Reinforced Nitrocellulose Blotting Membrane). Each membrane was blocked with 5% dry milk in phosphate-buffer saline and 0.1% Tween-20 (PBST) for 1 h and then incubated with the indicated primary antibodies overnight at 4°C. The membranes were rinsed and incubated with peroxidase-conjugated secondary antibodies for 1 hour at RT. Immunoblotted membranes were developed with ECL™ Select western blot detection reagents (Amersham Biosciences, UK) and imaged on the ChemiDoc™ XRS imaging system (Bio-Rad). Image processing and densitometric quantification of the bands were performed using the Image Lab software. Protein expression was normalized against housekeeping protein, which served as an internal control of protein loading. Relative protein expression was then calculated by dividing the normalized intensity of the condition sample by the control.
Antibodies used for western blot analysis are listed in **Table S7**. The corresponding anti-mouse and anti-rabbit secondary antibodies were used at 1:10000 dilutions.

**Protein half-life by cycloheximide chase assay**
6 x $10^5$ HCT116 cells with the three genotypes were seeded in a 6-well plate format. After 24 hours, cells from the first timepoint (t0) well were collected by trypsinization. The cell pellet was resuspended in 50 µl of RIPA lysis buffer prepared *as in the Western Blot section* and supplemented with 1X protease inhibitors (Roche). In the meantime, the media was aspirated from the remaining wells and replaced with 100 ug/ml of cycloheximide (Cayman Chemical) in 2 ml of fresh media to prevent further protein synthesis. After 10 minutes, 20 minutes, 30 minutes, and 1 hour from the treatment, cells were pelleted from the wells of the corresponding timepoints and resuspended in RIPA buffer 1X as well. Once all the pellets were harvested, proteins were extracted by centrifugation at 15000 rpm for 20 minutes at 4°C, quantified by the Bicinchoninic Acid Assay (Thermo Scientific™ Pierce™ BCA Protein Assay Kit), and Western Blot was performed as described earlier. 35 ug of timepoint t0 protein extract from each HCT116 clone was used in Western Blot. For timepoints > t0, the protein amounts were loaded volumetrically to the reference t0, for each clone. DDIT4 and β-Tubulin antibodies were used as primary antibodies. Mouse secondary antibody was used for both the primary antibodies. β-Tubulin was found to be a stable protein and thus was used as a loading control even in this context. Upon normalization of each DDIT4 band intensity to that of the corresponding β-Tubulin, relative protein abundance over time was calculated to the start of translation inhibition (t0) for each HCT116 clone.

**Global Translation by Click-iT® metabolic labelling of proteins**
Global translation was measured by using the Click-iT™ Plus OPP Alexa Fluor™ 488 Protein Synthesis Assay Kit according to the manufacturer's instructions. The fluorescence was measured by the ImageXpress High-Content imaging system (Molecular Devices).

**Global translation by Puromycin incorporation assay**

6 x $10^5$ HCT116 cells with the three genotypes were seeded in a 6-well plate format. When the cells reached 60% confluence, they were treated with vehicle or 100nM Thapsigargin for 4 or 16 hours. 1µM puromycin was added for 30 min at 37°C prior to pellet collection. Cycloheximide 100 µg/ml was used as a positive control. The cells were lysed, and the puromycin incorporation was assayed by western blot as described above. Stain-free intensity was measured as the reference.

**Cell proliferation assay**

HCT116 DDIT4 edited clones were seeded at 2.5 x $10^3$ per well onto 96-well plates and incubated at 37°C in standard conditions. The cell number was followed by the high content fluorescent microscope Operetta (PerkinElmer) in digital phase contrast every 24h for 96 h.

**RNA immunoprecipitation-qPCR (RIP-qPCR)**

8 x $10^6$ HCT116 cells from edited clones were seeded in 150 mm cell culture dishes (Sarstedt) and harvested after 48 hours by scraping. Cells were lysed in 800 µl of mild lysis buffer (20 mM HEPES pH 7.9, 150 mM NaCl, 1% Triton-X 100, 10% glycerol, 1 mM $MgCl_2$, 1 mM EGTA, 100 U/mL RNasin (Promega), 1X protease inhibitors (Roche)). After 30 minutes of incubation on ice, the lysate was obtained by centrifugation at 15000 rpm, 4°C for 10 minutes. The protein amount was quantified by the Bicinchoninic Acid Assay (Thermo Scientific™ Pierce™ BCA Protein Assay Kit). Meantime, 20 µl of Protein A Dynabeads (Invitrogen™) per condition were washed twice with 500 ul of IPP500 buffer (20 mM HEPES pH 7.4, 500 mM NaCl, 1.5 mM $MgCl_2$, 0.5 mM DTT, 0.05% NP40) and incubated with either 0.22 µg of anti-RBMX/hnRNP G antibody (#14794, 1:40, Cell Signaling Technology®) or 0.22 µg of anti-Normal Rabbit IgG antibody (#2729, Cell Signaling Technology®) in 100 µl of IPP500 buffer for 1h 30 at room temperature in a rotating wheel. After antibody conjugation, beads were further washed once with 900 µl of IPP500 buffer and twice with 900 µl of IPP150 1x buffer (20 mM HEPES pH 7.4, 150 mM NaCl, 1.5 mM MgCl2, 0.5 mM DTT, 0.05% NP-40) and once with PBS. Nonspecific binding was blocked by incubating the beads with 300 µl of 10 mg/ml Bovine Serum Albumin (BSA) for 30 minutes at room temperature in a rotating wheel. Beads were further washed three times with 800 µl of IPP150 1X buffer and incubated with 1 mg of the protein lysate in IPP150 1X buffer and 1x protease inhibitors in a final volume of 400 µl O/N at 4°C in a rotating wheel. Before the incubation with the beads, 10% of lysate in IPP150 1X buffer was isolated as protein input for Western Blot analysis, and 1% was isolated as RNA input for qPCR analysis. After O/N incubation, the flow-through (unbound lysate) was collected for Western Blot analysis, the beads were washed four times with 800 µl of IPP150 1X buffer, and 10% of the last wash was also collected for Western Blot analysis upon elution in LB 1X (Laemmli Sample Buffer, Bio-Rad) heating at 98°C for 10 minutes. Conversely, elution both for RIP samples (beads) and RNA inputs was performed by incubation with 5 µl of >600 U/ml proteinase K solution (Qiagen) and 150 ul of Proteinase K buffer (20 mM Tris-HCl pH 7.4, 10 mM $MgCl_2$, 0.2% Tween-20) at 55°C for 30 minutes in a lab heat block shaking at 700 rpm. The output RNA is extracted with TRIzol® reagent (Invitrogen™) according to the manufacturer's instructions. The total amount of eluted RNA was retrotranscribed using the RevertAid First Strand cDNA Synthesis Kit (Thermo Scientific™) and 1 µl of cDNA in 10 µl of reaction was used in the following RT-qPCR analysis with the qPCRBIO SyGreen Mix (PCR Biosystems) and the QuantStudio™ 5 Real-Time PCR System (Applied Biosystems®) instrument. Primers are listed in Table S4.

**RNA Electromobility Shift Assay (REMSA)**

The interaction between DDIT4 mRNA and RBMX protein was assessed *in vitro* by REMSA. The full-length recombinant RBMX protein was purchased from Origene (TP710403). FAM-labelled fluorescent RNA probes (GAGGGACUGAUUCCU/AGUGGUUGGAA-3'FAM) for the T and A alleles were purchased from Metabion. The binding reaction was set up in 10 µl in the following

binding buffer (10 mM HEPES, 50 mM KCl, 1 mM EDTA, 0,05% NP-40, 10% Glycerol, 0,5 mM DTT, pH 11.5). 10 U of RNasin (1 µl) were also added to each reaction and incubated for 30 minutes at RT in the dark. Upon incubation, 1 µl of 6X Orange Dye was added to each reaction to facilitate the visualization of the samples. The binding complex was resolved by running this reaction on a 6% TBE polyacrylamide native (non-denaturing) gel at 80V for 1 hour in TBE 1X at RT. The gel was pre-run in cold TBE 0.5X at 100V for 30 minutes and imaged using the SYBR filter in the ChemiDoc™ XRS imaging system (Bio-Rad).

**Cell Fractionation**

Cell fractionation was performed using a 0,1% Igepal buffer in PBS 1X as in the REAP fractionation protocol (Suzuki et al. 2010) coupled with an RNA extraction protocol (Gagnon et al. 2014) to improve the extraction of the RNA from the nuclei. Briefly, HCT116 TT and AA clones were seeded in 10-cm dishes. Once confluent, cells were detached by trypsinization, washed with PBS, and lysed in 900 µl of ice-cold 0,1% Igepal buffer in PBS 1X buffer for 2 minutes; 300 µl of this lysate were removed as whole cell lysate (WCL). The lysate was then fractionated by centrifugation at 12000 rpm for 40s, at RT. 300 µl of the supernatant were isolated as a cytoplasmic fraction (CYTO). The pellet was washed with 1 ml of 0.1% Igepal buffer and centrifuged at 12000 rpm for 40s, at RT to obtain the nuclear fraction. 50 µl out of 300 µl were isolated from each fraction for Western Blot analyses upon further lysis by RIPA buffer. The remaining 250 µl were used for TRIzol-based RNA extraction. To implement RNA extraction, the CYTO and NUCLEI fractions were resuspended in 1 ml of TRIzol. Lower volumes of TRIzol did not successfully extract RNA in our conditions. RNA was incubated for 10 minutes in TRIzol at RT, then 10 µl of EDTA 0.5 M were added before incubation at 65C for 5 min, 600 rpm (or until the pellet was completely dissolved). Subsequently, chloroform was added to follow the conventional TRIzol protocol.

**RBMX Silencing**

HCT116 TT and AA cells were transfected with a single or a mixture of two out of three siRNAs targeting RBMX (IDT) at a final concentration of 40 nM for 48 hours (**Table S4**). Control cells were transfected with a non-targeting siRNA (IDT, 51-01-14-04) in the same conditions. INTERFERin® (Polyplus) was used as a transfection reagent.

**Xenograft of HCT116 cells in zebrafish larvae**

**Animal rearing:** Zebrafish (*Danio rerio*) strains were raised and maintained in the Model Organism Facility (MOF) at the Department CIBIO, University of Trento under standard conditions (Kimmel et al. 1995). The transgenic zebrafish line *Casper* (White et al. 2008) was used to acquire live images in transparent larvae. All zebrafish studies were performed according to European and Italian law, D.Lgs. 26/2014, authorization11/2023-PR to MM.

**Larvae preparation:** Embryos were initially maintained at 28 ◦C at a maximum density of 50 embryos per Petri dish in fish water supplemented with 0.0002% methylene blue (Sigma, Burlington, MA, USA) as an antifungal agent. After 24 h, embryos were placed in fish water without methylene blue.

**Xenotransplantation of human cancer cell lines:** the protocol of xenotransplantation procedure was adapted from (Marines et al. 2023; Lorenzini et al. 2023). GFP or RFP labeled HCT116 cells (edited AA, TT, and AT clones) were harvested from a 100 mm Petri dish on the day of xenotransplantation and resuspended in 70 ul of PBS. 0.5 µL of cell suspension containing 200-400 cells was transplanted in the swim bladder of 2 dpf zebrafish larvae anesthetized in 0.16 mg/ml PBS/Tricaine (MS-222) under a Nikon SMZ800 stereomicroscope, using a micromanipulator

(Marzhouser Wetzkar MM 33 links) and the manual microinjector (CellTram® 4r Air Eppendorf). Transplanted embryos were maintained at 33°C in fish water. Larvae were selected for good transplantation profile using a Leica MZ 10F fluorescence stereomicroscope.

**Live-imaging and image analysis:** each larval xenograft was imaged one day post-transplantation (D1) and 3 days post-transplantation (D3) using Leica TCS SP8 laser scanning confocal system (CD7) (Objectives: 10x/1). Images were acquired in z-stack mode with a z-step interval of 7 µm to a range of 170-230 µm depending on the tumor size. The 488/633 nm lasers were used with appropriate filters to acquire green and red fluorescent cancer cells. Image analysis was performed using Fiji software. To study tumor growth of cancer cells *in vivo*, the maximum projection of every image was created, and a threshold was applied for each larva on day 1 (D1) and day 3 (D3) to generate a mask of the tumor area. The area on D3 was normalized to the area of D1 to assess the percentage of tumor growth for each larva.

**Single-molecule inexpensive RNA fluorescence in situ hybridization**

The smiFISH protocol was adapted from (Querido et al. 2020). Cells were grown on 22 × 22 mm glass coverslips (Prestige) previously stripped with 1 M HCl, sterilized, and stored in 100% ethanol. Cells were fixed in 4% paraformaldehyde (PFA) (Electron Microscopy Science) for 20 min at room temperature and then washed two times with 1× PBS. Permeabilization was performed in 0.5% Triton X-100, 1× PBS for 5 min at room temperature. Once permeabilized, samples were incubated at room temperature in a solution containing 1× SSC and 15% formamide, for 40 min and placed cell-side down on a 50-µl drop of hybridization buffer containing the probe [1× SSC, 15% formamide, bovine serum albumin (BSA) (4.5 mg/ml), 10.6% dextran sulfate, 2 mM Vanadyl Ribonucleoside Complex (VRC), yeast tRNA (0.4 mg/ml), 1 µl of probe mix] in an air-tight hybridization chamber protected from light overnight at 37°C. The probe mix preparation is described in the next paragraph. The following day, coverslips were washed twice with prewarmed 1× SSC solution containing 15% formamide for 30 min at 37°C. After that, coverslips were rinsed twice with 1× PBS, cells were stained with DAPI (1 ng/µl) (4′,6-diamidino-2-phenylindole) in 1× PBS, for 12 min at room temperature and washed with 1× PBS. Samples were mounted on precleaned glass slides using ProLong Diamond Antifade Mountant (Thermo Fisher Scientific).

**smiFISH probe preparation**

Probe preparation was performed as described by (Querido et al. 2020). For DDIT4 detection, 3 primary probes targeting the DDIT4 sequence were used and prepared as a 20 µM equimolar mixture in milliQ water. Sequences of the probes are shown in Table S4. Primary probes were mixed with 50 pmol of fluorescently labeled secondary probes in 1× NEB3 solution [100 mM NaCl, 50 mM tris-HCl (pH 8), 10 mM MgCl2] in a final volume of 10 µl. Primary probes were annealed with secondary probes in a PCR thermocycler (85°C for 3 min, 65°C for 3 min, 25°C for 5 min. As described in the previous paragraph, the probe mix (1 µl) was used for the smiFISH hybridization buffer preparation.

**smiFISH combined with IF**

For smiFISH/IF experiments, the smiFISH technique was performed first, using the protocol described in the smiFISH paragraph, and followed by the immunofluorescence protocol as described hereafter. After the overnight probe hybridization, cells were washed twice in prewarmed 1× SSC, 15% formamide solution. After two rinses in 1× PBS, cells were incubated in blocking solution (1× PBS, 2% BSA, 0.1% Triton X-100) for 3 hours and incubated for 1 hour at room temperature with the primary antibody diluted in blocking solution. For RBMX detection, we used the antibody in Table S7 at 1:200 dilution. Cells were then washed five times for 6 min with 1× PBS, 0.1% Triton X-100, and incubated with the appropriate fluorescent secondary antibody for 1 hour [goat anti-rabbit

Alexa Fluor 488 (AF488), from Thermo Fisher Scientific, catalog no. A-11034, 1:1500 dilution; donkey anti-mouse AF647, from Thermo Fisher Scientific, catalog no. A-31571, 1:1000 dilution]. After incubation, cells were washed five times for 6 min with 1× PBS, 0.1% Triton X-100, and stained with DAPI (1 ng/µl) in 1× PBS for 12 min. After two washes with 1× PBS, coverslips were mounted on glass slides using ProLong Diamond Antifade Reagent (Thermo Fisher Scientific).

**smiFISH/IF image acquisition by confocal microscopy**

Images were acquired using a confocal laser scanning Leica TCS SP8 inverted microscope (Leica Camera AG) with a plan apochromatic 63×/1.40 oil immersion objective and 2× zoom. Normal photomultipliers (PMTs) were used to detect DDIT4 smiFISH signal, RBMX, b-tubulin, and DAPI signals. Optimal acquisition parameters, including nanometer range of excitation, gain, offset, and laser power, were optimized for the visualization of each fluorophore at the beginning of the acquisition and maintained throughout each experiment. Z stack images were acquired in each experiment with a 0.3-µm step and 2048 × 2048 pixel size resolution using Leica Application Suite X (LAS X) imaging software.

**Confocal image analysis**

Images were analyzed using CellProfiler 4.0.7 (Broad Institute, Inc.). Briefly, cell nuclei were identified as the primary object using the DAPI signal. For each object, the cellular region was defined by propagating from the nucleus, applying a low segmentation threshold to the smoothed smiFISH signal. The cytoplasm was defined as a tertiary object by subtracting the nuclear masks from the cellular regions. DDIT4 smiFISH signal spots were segmented as objects with a typical diameter range of 10 to 30 pixels. Subsequently, objects were localized based on their position relative to the nuclear or cytoplasmic regions. Since the majority of the spots exhibited a perinuclear localization, the nuclear regions were reduced by 5% to prevent misleading classification. Morphological features and intensity values for both DDIT4 smiFISH and RBMX signals were calculated at the object level.

**Immunohistochemistry**

Briefly, three-micron sections from paraffin blocks by seven patients with colon adenocarcinoma were cut and incubated (37°C overnight). IHC staining was performed using Bond III IHC autostainer for full Automated Immunohistochemistry (Leica Biosystems). Antigens were unmasked with Bond Epitope Retrieval Solution 1 Leica AR9961 and incubated with the following antibody (diluted with Bond Primary Antibody Diluent, AR9352 Leica): DDIT4/REDD1 at dilution 1:400 (Proteintech 10638-1-AP). Samples were stained with BOND IHC Polymer Detection Kit (DS9800) and counterstained using Hematoxylin solution (Leica). The IHC score was obtained by analyzing the slides by a certified pathologist (G.B.) and applying also ImageJ, a digital image processing software. Informed consent was obtained from all patients for the use of tissue materials for research purposes.

**Statistical analysis**

Results were plotted and statistically analyzed using GraphPad Prism, version 10. The statistical test applied, the number of replicates, and the level of significance is provided in each figure legend.

## Supplementary Figures and Tables

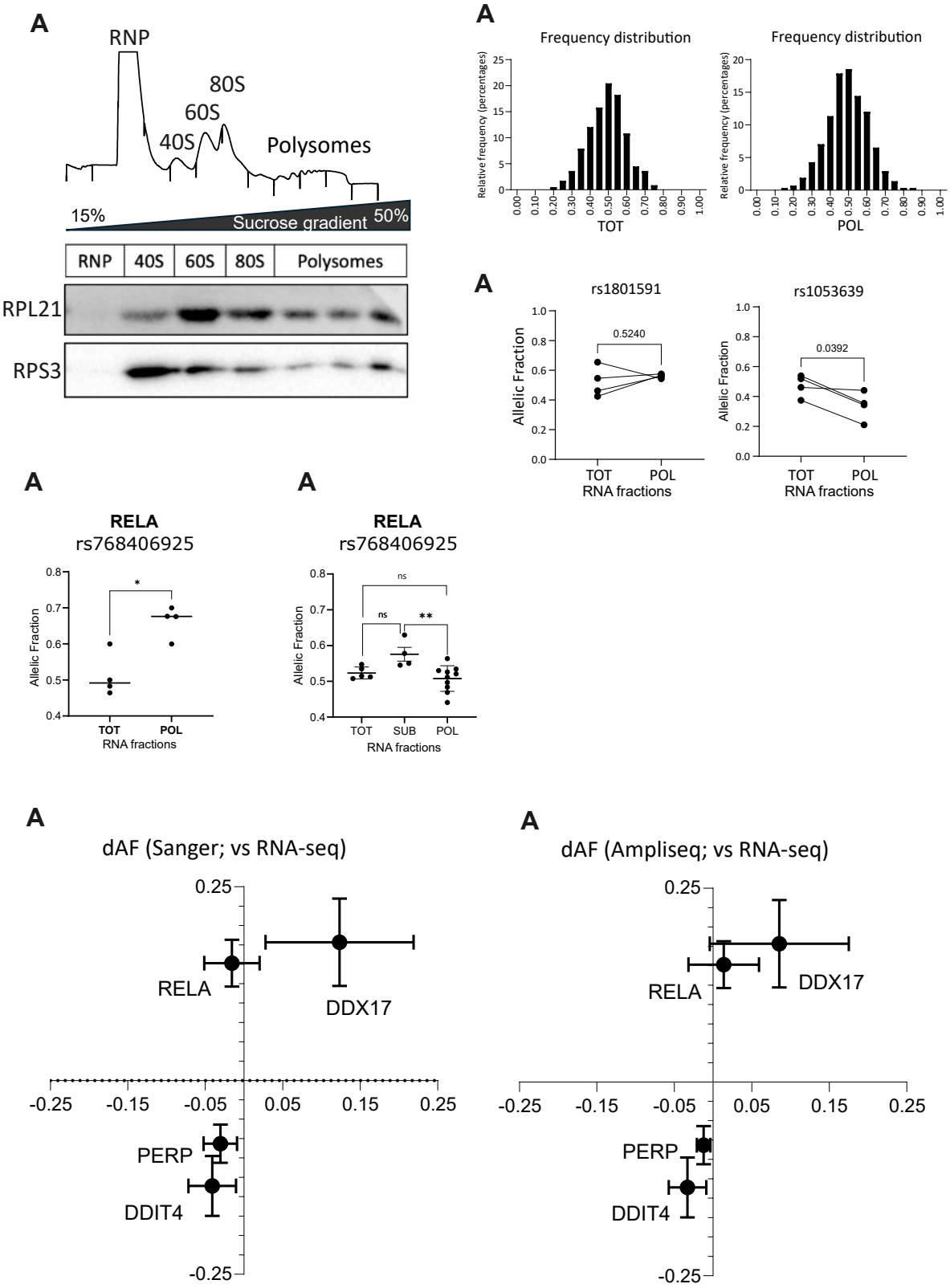


**Figure S1A. TranSNPs identification and validation -**related to Figure 1-.

**A)** Representative polysome profile of HCT116 cells and western blot results for markers of the small (RPS3) and large (RPL21) ribosomal subunits used as controls for sedimentation. Lysates separated to equilibrium density by ultracentrifugation on a linear 15-50% sucrose gradient were fractionated following UV absorbance recorded at 254 nm. The fractions representing polysomes (POL) that were pooled together for subsequent analysis are indicated. **B**) Distribution

plotted as the percentage of the relative frequency of average allelic fractions for all the heterozygous SNPs that could be studied in the RNA-seq experiment, for total (left figure) and polysomal (right figure) RNA. AF data for each of the four experimental replicates is provided in Table S1. The RNA-seq dataset is deposited in GEO (accession number: GSE95024). **B**) Examples of paired t-test statistics exploited to assess the concordance of differential AF measures across pairs of polysomal and total RNA biological replicates. **D**) Plots of the allelic fraction (the number of alternative allele reads divided by the sum of alternative and reference allele reads) measured for rs768406925 in the RELA gene from RNA-seq results obtained in total cytoplasmic lysates (TOT) or pooled polysomal fractions (POL). **E**) Allelic fraction measurements obtained by Sanger sequencing and electropherogram quantification from independent biological replicates of polysome profiling experiments in HCT116 cells for rs768406925 in RELA. **F**) Correlation between delta allelic fractions measured for the SNPs in the four indicated genes using RNA-seq (Y-axis) or Sanger electropherograms (X-axis). The average and standard deviations of replicates are plotted. **G**) Correlation graph as in F, focusing on the RNA-seq data (Y-axis) and the results obtained by Ampliseq-based targeted resequencing (X-axis).

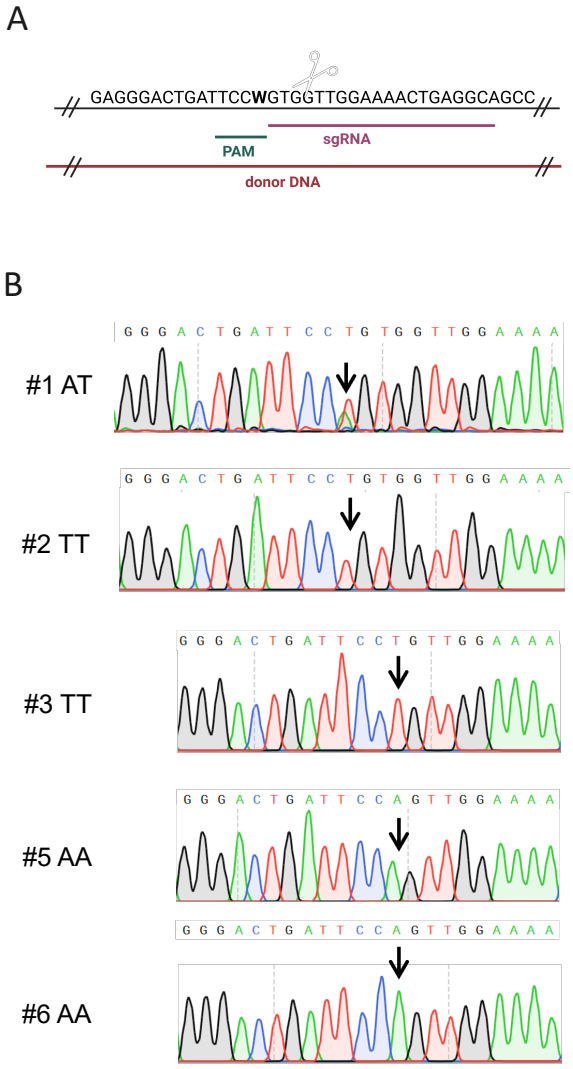


**Figure S2. Editing of HCT116 cells to obtain the three genotypes for the rs1053639 T/A SNP.**
Parental HCT116 cells - heterozygous for the rs1053639 SNP - were edited to obtain homozygous clones for the A and the T alleles. **A)** CRISPR/Cas9-mediated knock-in was employed for this aim. We annealed a gene-specific crRNA with a tracrRNA, obtaining a sgRNA for DDIT4. The same sgRNA cut both alleles since the SNP represented the "N" base of the -NGG PAM. An 85-nt long donor DNA with the endogenous sequence (mixture of 50% A and 50% T) was purchased to be used as a template. **B)** Representative electropherograms of Sanger sequencing analyses indicating the genotype of the selected clones for rs1053639.

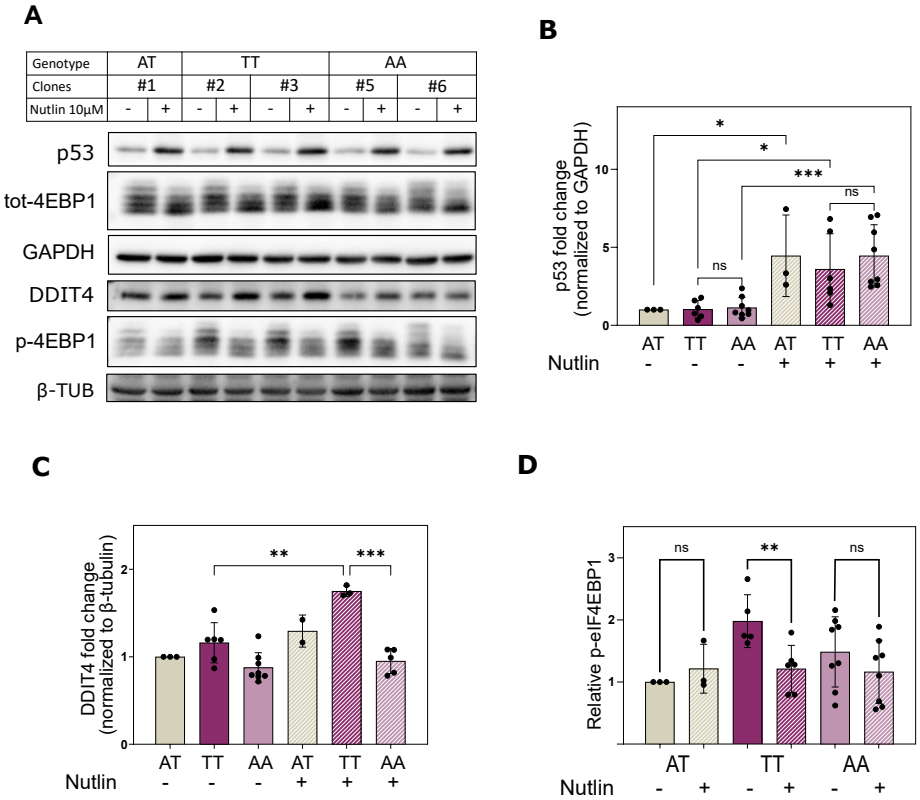


**Figure S3. The rs1053639 tranSNP genotype impacts on mTOR pathway markers upon Nutlin. treatment.** HCT116 parental cells and clones differing for the rs1053639 homozygous genotypes were treated with either Nutlin 10 µM or vehicle control for 16 hours. **A)** Cell lysates were analyzed by immunoblotting for the induction of p53 and DDIT4 protein levels and the phosphorylation state and levels of the eIF4EBP1 mTORC1 target. β-Tubulin and GAPDH were used as references. **B, C)** Densitometry analysis of p53 and DDIT4 protein levels shows significant induction upon Nutlin treatment. **D)** Densitometry analysis of phosphorylated eIF4EBP1 blots reveals that significant inhibition of the phosphorylation of eIF4EBP1 is apparent only in the rs1053639 TT homozygous clones. ***p-value <0.005. **p-value <0.001. *p-value <0.05. ns, not significant. unpaired t-test.

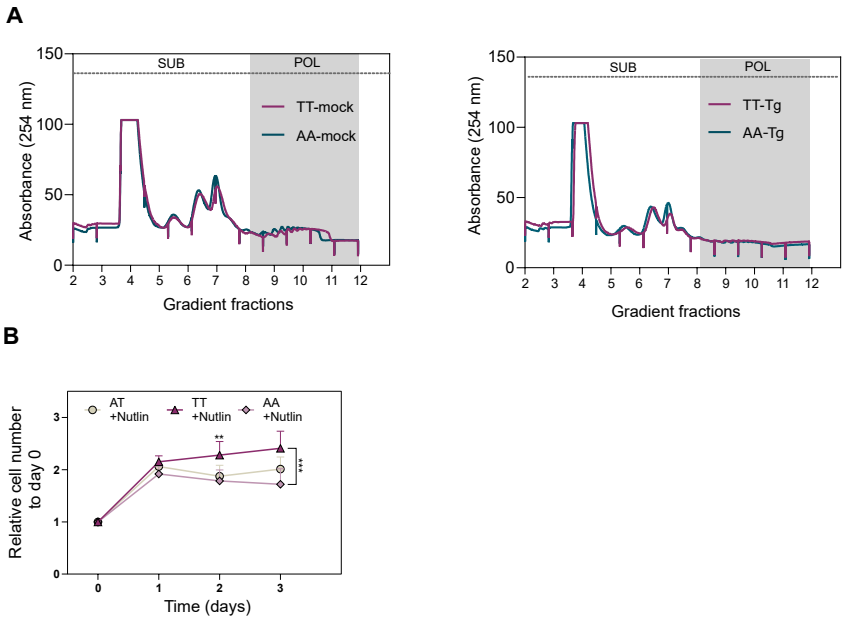


**Figure S4. The DDIT4 rs1053639 genotype does not strikingly impact global translation and cell proliferation in response to cellular stresses.**

**A)** Representative polysome profiles of HCT116 TT and AA clones treated with vehicle (Left) or thapsigargin 100nM for four hours (Right). Lysates separated by ultracentrifugation on a linear 15-50% sucrose gradient were fractionated following

UV absorbance recorded at 254 nm. The fractions representing RNA complexes used for subsequent analysis are indicated in the figure. **B)** HCT116 cells with the three genotypes differing for the rs1053639 were treated with 5µM Nutlin for 72 hours. The sensitivity of the clones was followed every 24 hours by the Operetta HCS system. Relative cell number curves were plotted as the mean of several replicates ± standard deviation (SD). ***p-value <0.0005. Ordinary two-way ANOVA.

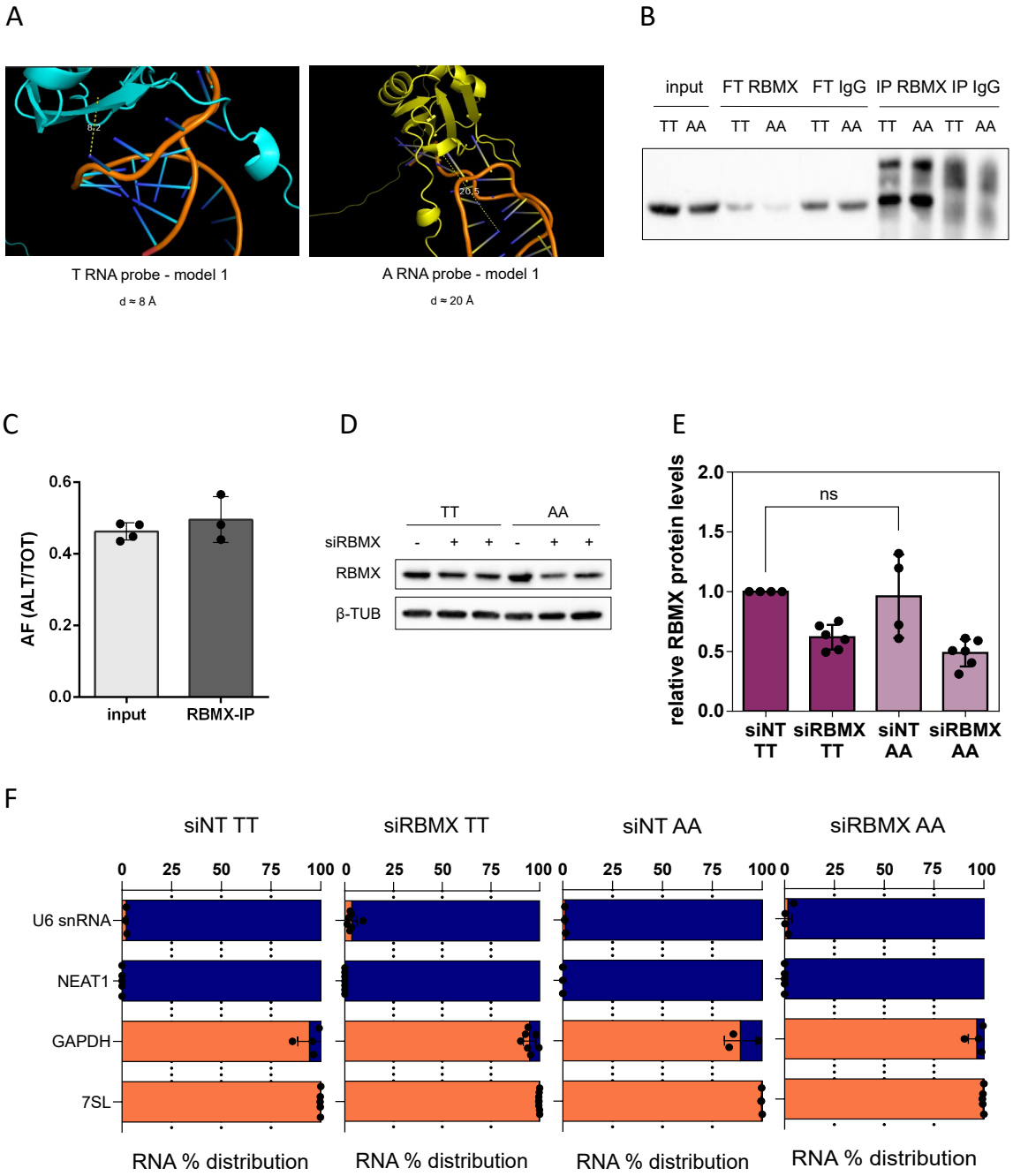


**Figure S5. The rs1053639 tranSNP genotype impacts mRNA fate through the RBMX protein.**
**A)** AlphaFold3 was used to predict the interactions between the full-length RBMX protein and the RNA probes (A, T) used for the RNA EMSA. Four models were explored, model 1 is shown as representative. The tool allows the calculation of the distance between a selected RNA nucleotide and a selected protein portion. The distance between the T SNP nucleotide and the RBMX protein was lower than the distance between the A SNP nucleotide and the same protein in all four models. **B)** RBMX was specifically immunoprecipitated across TT and AA cells with similarly high efficiencies. An IgG control antibody of the same species as the anti-RBMX antibody was used as a control for specificity. FT: flow-through, unbound lysate upon IP. **C)** The endogenous RBMX protein was immunoprecipitated either from a whole cell lysate or from a nuclear extract in heterozygous parental HCT116 cells. RNA from the input and IP samples was extracted and retro-transcribed. The cDNA was amplified by performing RT-qPCR and submitted to Sanger sequencing. Results are indicated as the AF of the alternative allele (A) over the Total (A+T) and represent the mean ± SD of three independent experiments. **D, E)** TT

and AA clones were treated with either a mixture of siRNAs targeting RBMX or the siRNA control for 48 hours. Representative immunoblot and the densitometric analysis show that the RBMX protein is equally expressed independently from the rs1053639 and that the efficiency of RBMX silencing was similar across TT and AA clones. β-Tubulin was used as a loading control. **F)** Markers for RNA fractionation upon siNT or siRBMX. U6 snRNA and NEAT1 were used as markers of the nuclear fraction, and 7SL and GAPDH were used as markers of the cytoplasmic fraction.

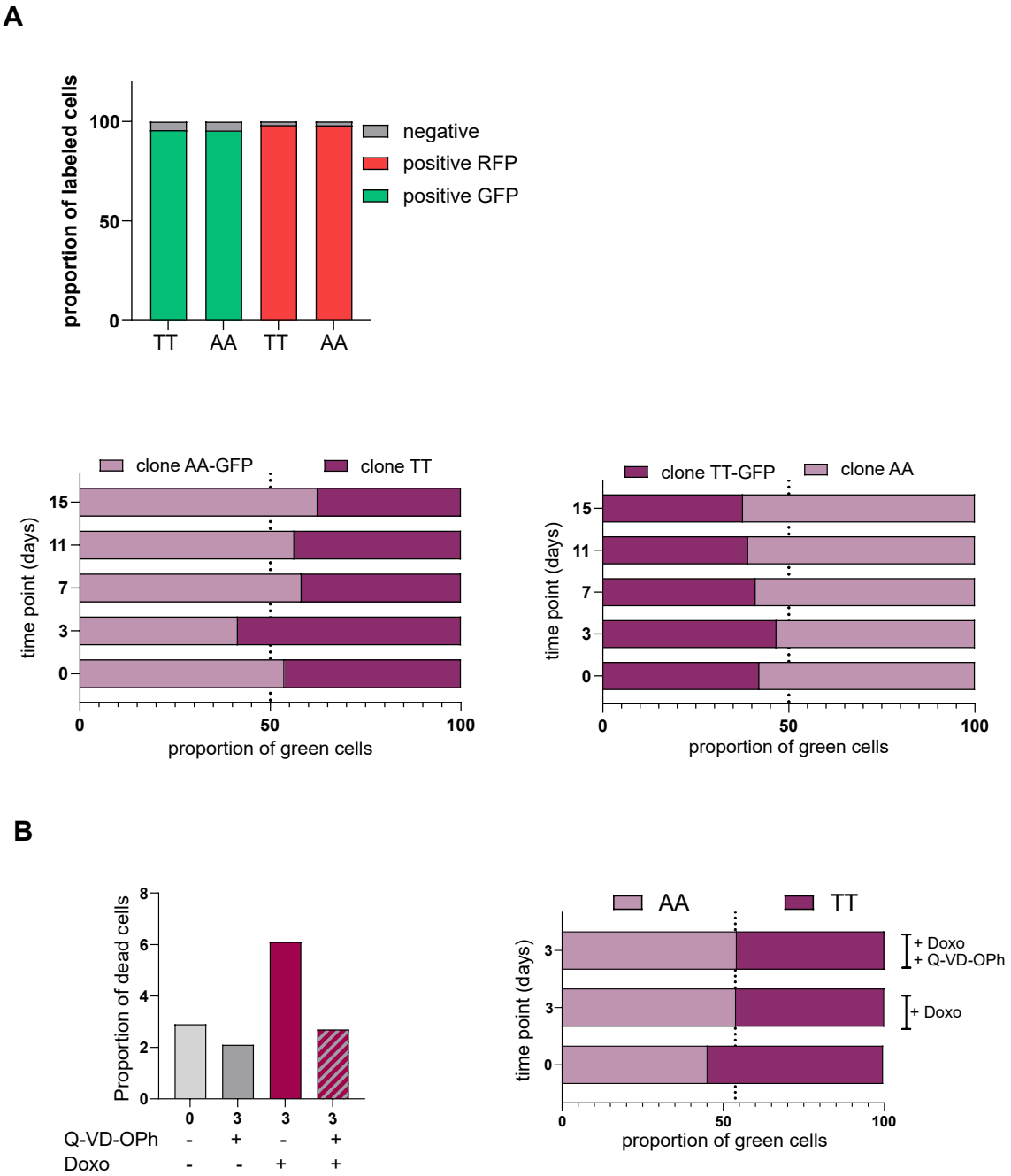


**Figure S6. The rs1053639 tranSNP AA genotype shows a competitive growth advantage in prolonged culture conditions.**

**A)** (Top) DDIT4 clones harboring the TT and AA genotypes were both separately transduced with Lentiviral particles to constitutively express either EGFP or MiRFP. After transduction, cells were treated with 5 µg/ml blasticidin for at least 15 days, to reach at least 95% of GFP+ or RFP+ cell populations. (Bottom) TT and AA clones were co-cultured using both combinations for the fluorophore. The graphs are representative of at least four replicates for each combination and show that the results were not influenced by the presence of the fluorescent marker.

**B)** HCT116 clones were treated with Doxorubicin 3µM to induce apoptosis prior to Q-VD-OPh as a positive control (Left). TT and AA in co-culture were treated with Doxorubicin and /or Q-VD-OPh. The graph represents the proportion of the GFP+ cells after three days acquired by FACS.

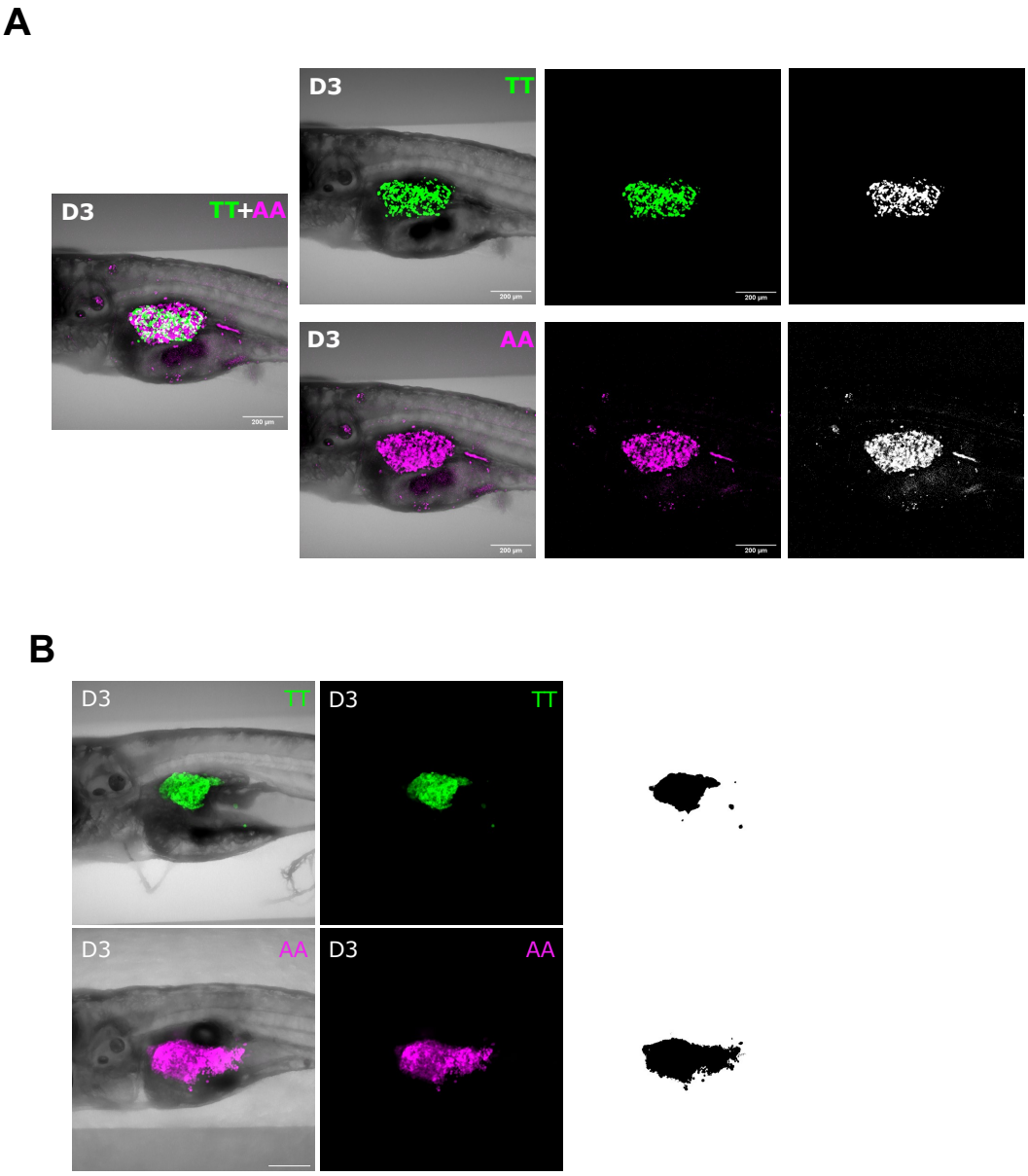


**Figure S7. DDIT4 rs1053639 impacts tumor growth and genotypic competition in zebrafish larvae xenotransplants.** Image analysis was performed by Fiji software, and quantification of the tumor growth was carried out by applying fixed thresholds for fluorescent intensity, as described in Materials and Methods. **A, B)** Representative images for both confocal and its corresponding Fiji quantification mask.

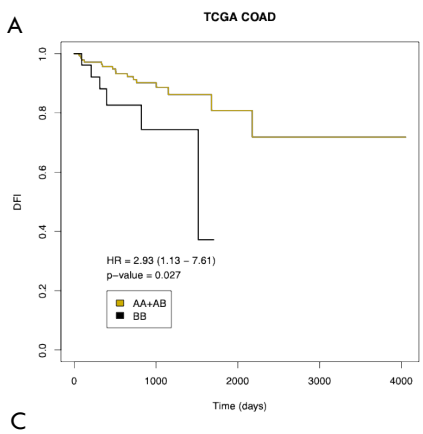


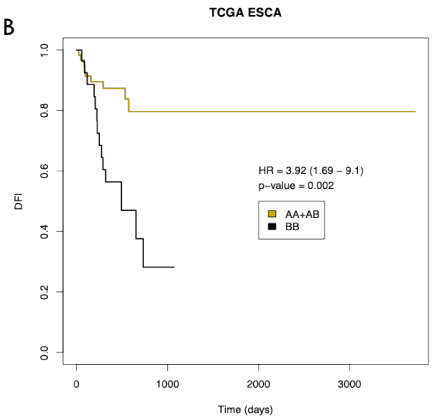


C

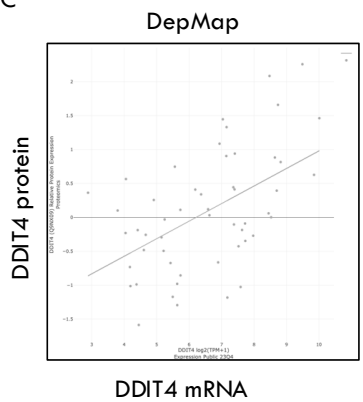


D

| IHC score: | High | | Low | |
|---|---|---|---|---|
| | Sample Code | DDIT4 rs1053639 genotype | Sample Code | DDIT4 rs1053639 genotype |
| Normal Tissue | 16-I-04747 | TT | 16-I-00016 | TT |
| | | | 16-I-02512 | TT |
| | | | 16-I-07061 | AT |
| | | | 15-I-26303 | AT |
| | | | 16-I-14809 | AA |
| | | | 16-I-25747 | AA |
| | | | | |
| Tumor Tissue | 16-I-04747 | TT | 16-I-00016 | TT |
| | 16-I-14809 | AA | 16-I-02512 | TT |
| | 16-I-25747 | AA | 16-I-07061 | AT |
| | | | 15-I-26303 | AT |

E

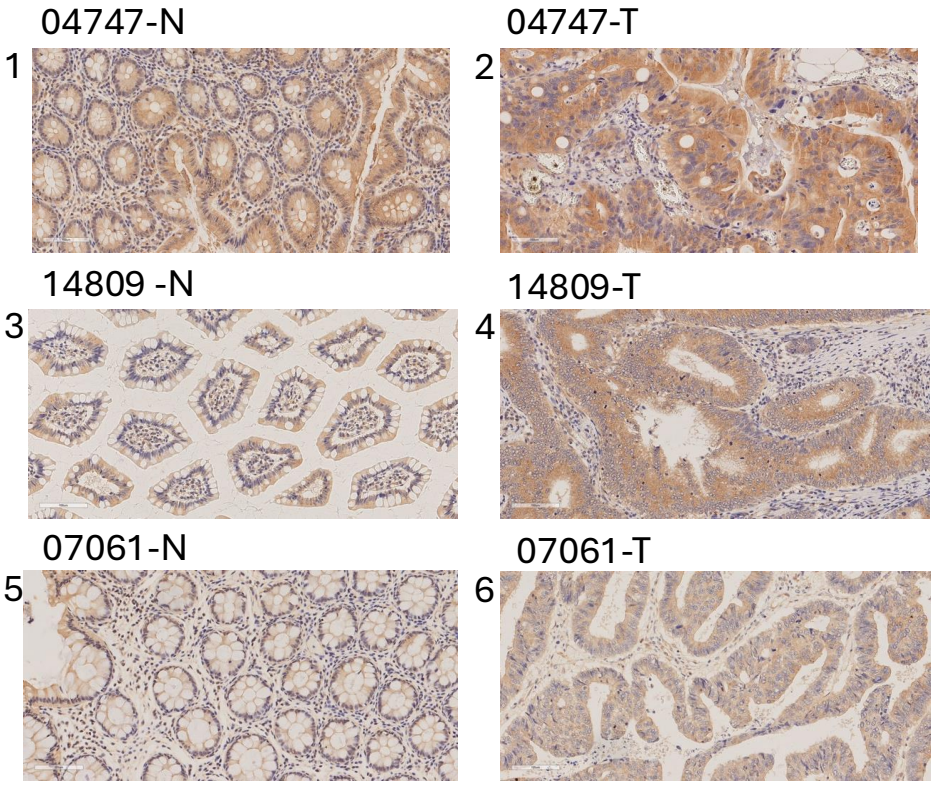


**Figure S8. Exploration of the prognostic value of rs1053639 genotype.**
**A-B)** Survival probability from TCGA data plotted after stratifying patients based on the rs1053639 genotype and under a recessive model (A = reference allele (T); B = alternative allele (A)). **C)** Correlation between DDIT4 protein and mRNA levels in cancer cell lines from the DepMap database. **D)** Genotyping results for rs1053639 in seven colon cancer samples. The IHC score was obtained by analyzing the slides by two certified pathologists and applying also a custom script in Fiji -see methods-. **E)** Representative images of IHC DDIT4 staining. -N and -T after the sample code refer to normal colon mucosa or cancer tissue, respectively. The sensitivity of IHC staining was verified by paraffin embedding pellets from our edited HCT116 cell clones (not shown). Images of sample 04747-N and -T, genotype TT, show high expression of

cytoplasmic DDIT4 (E1 and E2). Sample 14809-N, genotype AA, shows a low expression of cytoplasmic DDIT4 (E3), while the 14809-T tumor counterpart shows high expression (E4). Finally, images of sample 07061-N and -T, genotype AT, both show low cytoplasmic expression of the DDIT4 protein (E5 and E6).

**Table S1.** List of analyzable heterozygous SNPs in HCT116 RNA-seq dataset

**Table S2.** List of the tranSNPs identified. ID, gene name, location, and AF data are reported

**Table S3.** RNA-binding protein binding predictions for rs1053639.

**Table S4**. Sequences of primers and siRNAs

**Table S5**. Sequence of crRNA and donor DNA sequences and summary of the efficiency of the CRISPR/Cas9-mediated HDR.

**Table S6**. Summary table of the genotypes of selected rs1053639 edited clones.

**Table S7**. Table of the antibodies used in this study.

**Table S8**. Comparison of the expression of tranSNP host genes in colon adenocarcinomas and controls, based on TCGA data.

## References


Bolger AM, Lohse M, Usadel B. 2014. Trimmomatic: a flexible trimmer for Illumina sequence data. *Bioinformatics* **30**: 2114–2120. http://www.ncbi.nlm.nih.gov/pubmed/24695404.

Bowling S, Di Gregorio A, Sancho M, Pozzi S, Aarts M, Signore M, Schneider MD, Barbera JPM, Gil J, Rodríguez TA. 2018. P53 and mTOR signalling determine fitness selection through cell competition during early mouse embryonic development. *Nat Commun* **9**.

Brinkman EK, van Steensel B. 2019. Rapid Quantitative Evaluation of CRISPR Genome Editing by TIDE and TIDER. In *Methods in Molecular Biology*, Vol. 1961 of, pp. 29–44, Humana Press Inc.

Brugarolas J, Lei K, Hurley RL, Manning BD, Reiling JH, Hafen E, Witters LA, Ellisen LW, Kaelin WG. 2004. Regulation of mTOR function in response to hypoxia by REDD1 and the TSC1/TSC2 tumor suppressor complex. *Genes Dev* **18**.

Chen R, Wang B, Chen L, Cai D, Li B, Chen C, Huang E, Liu C, Lin Z, Xie WB, et al. 2016. DNA damage-inducible transcript 4 (DDIT4) mediates methamphetamine-induced autophagy and apoptosis through mTOR signaling pathway in cardiomyocytes. *Toxicol Appl Pharmacol* **295**.

Chen X, Li Z, Liang M, Zhang Z, Zhu D, Lin B, Zhou R, Lu Y. 2023. Identification of DDIT4 as a potential prognostic marker associated with chemotherapeutic and immunotherapeutic response in triple-negative breast cancer. *World J Surg Oncol* **21**.

Clamer M, Tebaldi T, Lauria F, Bernabò P, Gómez-Biagi RF, Marchioretto M, Kandala DT, Minati L, Perenthaler E, Gubert D, et al. 2018. Active Ribosome Profiling with RiboLace. *Cell Rep* **25**.

Conant D, Hsiau T, Rossi N, Oki J, Maures T, Waite K, Yang J, Joshi S, Kelso R, Holden K, et al. 2022. Inference of CRISPR Edits from Sanger Trace Data. *Cris J* **5**.

Cook KB, Kazan H, Zuberi K, Morris Q, Hughes TR. 2011. RBPDB: A database of RNA-binding specificities. *Nucleic Acids Res* **39**: D301-8.

Coronel L, Häckes D, Schwab K, Riege K, Hoffmann S, Fischer M. 2022. p53-mediated AKT and mTOR inhibition requires RFX7 and DDIT4 and depends on nutrient abundance. *Oncogene* **41**.

Dassi E, Zuccotti P, Leo S, Provenzani A, Assfalg M, D'Onofrio M, Riva P, Quattrone A. 2013. Hyper conserved elements in vertebrate mRNA 3'-UTRs reveal a translational network of RNA-binding proteins controlled by HuR. *Nucleic Acids Res* **41**: 3201–3216. http://www.ncbi.nlm.nih.gov/pubmed/23376935.

De La Chapelle A. 2009. Genetic predisposition to human disease: Allele-specific expression and low-penetrance regulatory loci. *Oncogene* **28**.

Dennis MD, Coleman CS, Berg A, Jefferson LS, Kimball SR. 2014. REDD1 enhances protein phosphatase 2A-mediated dephosphorylation of Akt to repress mTORC1 signaling. *Sci Signal* **7**.

Depristo MA, Banks E, Poplin R, Garimella K V., Maguire JR, Hartl C, Philippakis AA, Del Angel G, Rivas MA, Hanna M, et al. 2011. A framework for variation discovery and genotyping using next-generation DNA sequencing data. *Nat Genet* **43**.

Deyoung MP, Horak P, Sofer A, Sgroi D, Ellisen LW. 2008. Hypoxia regulates TSC1/2-mTOR signaling and tumor suppression through REDD1-mediated 14-3-3 shuttling. *Genes Dev* **22**.

DIas Louro MA, Peneda C, C. B, Bettencourt-Dias M. 2024. Adaptation of human cell populations to different levels of centriole amplification involves a two-step response. *bioRxiv Prepr*.

Dobin A, Davis CA, Schlesinger F, Drenkow J, Zaleski C, Jha S, Batut P, Chaisson M, Gingeras TR. 2013. STAR: Ultrafast universal RNA-seq aligner. *Bioinformatics* **29**.

Ellisen LW, Ramsayer KD, Johannessen CM, Yang A, Beppu H, Minda K, Oliner JD, McKeon F, Haber DA. 2002. REDD1, a developmentally regulated transcriptional target of p63 and p53, links p63 to regulation of reactive oxygen species. *Mol Cell* **10**.

Fang Y, Wu X, Gu Y, Shi R, Yu T, Pan Y, Zhang J, Jing X, Ma P, Shu Y. 2023. LINC00659 cooperated with ALKBH5

to accelerate gastric cancer progression by stabilising JAK1 mRNA in an m 6 A-YTHDF2-dependent manner . *Clin Transl Med* **13**.

Fattahi F, Saeednejad Zanjani L, Habibi Shams Z, Kiani J, Mehrazma M, Najafi M, Madjd Z. 2021. High expression of DNA damage-inducible transcript 4 (DDIT4) is associated with advanced pathological features in the patients with colorectal cancer. *Sci Rep* **11**.

Fu L, Cao Y, Wu J, Peng Q, Nie Q, Xie X. 2022. UFold: Fast and accurate RNA secondary structure prediction with deep learning. *Nucleic Acids Res* **50**.

Fujii K, Shi Z, Zhulyn O, Denans N, Barna M. 2017. Pervasive translational regulation of the cell signalling circuitry underlies mammalian development. *Nat Commun* **8**.

Gagnon KT, Li L, Janowski BA, Corey DR. 2014. Analysis of nuclear RNA interference in human cells by subcellular fractionation and Argonaute loading. *Nat Protoc* **9**.

Gandin V, Sikström K, Alain T, Morita M, McLaughlan S, Larsson O, Topisirovic I. 2014. Polysome fractionation and analysis of mammalian translatomes on a genome-wide scale. *J Vis Exp*.

Ghetti S, Burigotto M, Mattivi A, Magnani G, Casini A, Bianchi A, Cereseto A, Fava LL. 2021. CRISPR/Cas9 ribonucleoprotein-mediated knockin generation in hTERT-RPE1 cells. *STAR Protoc* **2**.

Goul C, Peruzzo R, Zoncu R. 2023. The molecular basis of nutrient sensing and signalling by mTORC1 in metabolism regulation and disease. *Nat Rev Mol Cell Biol* **24**.

Hamadou MH, Kerkatou M, Gatto P, Pancher M, Bisio A, Inga A, Menad A, Benayache S, Benayache F, Ameddah S. 2021. Apigenin rich-Limonium duriusculum (de Girard) Kuntze promotes apoptosis in HCT116 cancer cells. *Nat Prod Res* **35**.

Han S, Zhu L, Zhu Y, Meng Y, Li J, Song P, Yousafzai NA, Feng L, Chen M, Wang Y, et al. 2021. Targeting ATF4-dependent pro-survival autophagy to synergize glutaminolysis inhibition. *Theranostics* **11**.

He X, He L, Hannon GJ. 2007. The guardian's little helper: microRNAs in the p53 tumor suppressor network. *Cancer Res* **67**: 11099–11101. http://www.ncbi.nlm.nih.gov/entrez/query.fcgi?cmd=Retrieve&db=PubMed&dopt=Citation&list_uids=18056431.

Heinrich B, Zhang Z, Raitskin O, Hiller M, Benderska N, Hartmann AM, Bracco L, Elliott D, Ben-Ari S, Soreq H, et al. 2009. Heterogeneous nuclear ribonucleoprotein G regulates splice site selection by binding to CC(A/C)-rich regionsin pre-mRNA. *J Biol Chem* **284**.

Heyer EE, Moore MJ. 2016. Redefining the Translational Status of 80S Monosomes. *Cell* **164**.

Keoni CLI, Brown TL. 2015. Inhibition of apoptosis and efficacy of pan caspase inhibitor, Q-VD-OPh, in models of human disease. *J Cell Death* **8**.

Kimball SR, Jefferson LS. 2012. Induction of REDD1 gene expression in the liver in response to endoplasmic reticulum stress is mediated through a PERK, eIF2α phosphorylation, ATF4-dependent cascade. *Biochem Biophys Res Commun* **427**.

Kimmel CB, Ballard WW, Kimmel SR, Ullmann B, Schilling TF. 1995. Stages of embryonic development of the zebrafish. *Dev Dyn* **203**.

Kon N, Ou Y, Wang SJ, Li H, Rustgi AK, Gu W. 2021. mTOR inhibition acts as an unexpected checkpoint in p53-mediated tumor suppression. *Genes Dev* **35**.

Lee C, Kang EY, Gandal MJ, Eskin E, Geschwind DH. 2019. Profiling allele-specific gene expression in brains from individuals with autism spectrum disorder reveals preferential minor allele usage. *Nat Neurosci* **22**.

Leprivier G, Rotblat B. 2020. How does mTOR sense glucose starvation? AMPK is the usual suspect. *Cell Death Discov* **6**.

Liang S, Bellato HM, Lorent J, Lupinacci FCS, Oertlin C, van Hoef V, Andrade VP, Roffé M, Masvidal L, Hajj GNM, et al. 2018. Polysome-profiling in small tissue samples. *Nucleic Acids Res* **46**.

Liu C, Sun H, Yi Y, Shen W, Li K, Xiao Y, Li F, Li Y, Hou Y, Lu B, et al. 2023a. Absolute quantification of single-base m6A methylation in the mammalian transcriptome using GLORI. *Nat Biotechnol* **41**.

Liu J, Lichtenberg T, Hoadley KA, Poisson LM, Lazar AJ, Cherniack AD, Kovatich AJ, Benz CC, Levine DA, Lee A V., et al. 2018. An Integrated TCGA Pan-Cancer Clinical Data Resource to Drive High-Quality Survival Outcome Analytics. *Cell* **173**: 400–416.

Liu J, Zheng T, Chen D, Huang J, Zhao Y, Ma W, Liu H. 2023b. RBMX involves in telomere stability maintenance by regulating TERRA expression. *PLoS Genet* **19**.

Liu N, Zhou KI, Parisien M, Dai Q, Diatchenko L, Pan T. 2017. N6-methyladenosine alters RNA structure to regulate binding of a low-complexity protein. *Nucleic Acids Res* **45**.

Lorenz R, Bernhart SH, Höner zu Siederdissen C, Tafer H, Flamm C, Stadler PF, Hofacker IL. 2011. ViennaRNA Package 2.0. *Algorithms Mol Biol* **6**.

Lorenzini F, Marines J, Le Friec J, Do Khoa N, NIeto M, Sanchez-Laorden B, Mione M, Kissa K, Fontenille L. 2023. Melanoma innervation is associated with cancer progression in a zebrafish xenograft model. *bioRxiv Prepr* **doi:10.110**.

Malagelada C, Ryu EJ, Biswas SC, Jackson-Lewis V, Greene LA. 2006. RTP801 is elevated in Parkinson brain substantia nigral neurons and mediates death in cellular models of Parkinson's disease by a mechanism involving mammalian target of rapamycin inactivation. *J Neurosci* **26**.

Marcel V, Catez F, Diaz JJ. 2015. p53, a translational regulator: contribution to its tumour-suppressor activity. *Oncogene* **34**: 5513–5523. http://www.ncbi.nlm.nih.gov/pubmed/25728674.

Marcel V, Ghayad SE, Belin S, Therizols G, Morel AP, Solano-Gonzalez E, Vendrell JA, Hacot S, Mertani HC, Albaret MA, et al. 2013. p53 acts as a safeguard of translational control by regulating fibrillarin and rRNA methylation in cancer. *Cancer Cell* **24**: 318–330. http://www.ncbi.nlm.nih.gov/pubmed/24029231.

Marcel V, Van Long FN, Diaz JJ. 2018. 40 years of research put p53 in translation. *Cancers (Basel)* **10**.

Marines J, Lorenzini F, Kissa K, Fontenille L. 2023. Modelling 3D Tumour Microenvironment In Vivo: A Tool to Predict Cancer Fate. *Curr Issues Mol Biol* **45**.

Martin M. 2011. Cutadapt removes adapter sequences from high-throughput sequencing reads. *EMBnet.journal* **17**.

Panda A, Martindale J, Gorospe M. 2017. Polysome Fractionation to Analyze mRNA Distribution Profiles. *BIO-PROTOCOL* **7**: e2126.

Pringle ES, McCormick C, Cheng Z. 2019. Polysome Profiling Analysis of mRNA and Associated Proteins Engaged in Translation. *Curr Protoc Mol Biol* **125**.

Protiva P, Hopkins ME, Baggett S, Yang H, Lipkin M, Holt PR, Kennelly EJ, Bernard WI. 2008. Growth inhibition of colon cancer cells by polyisoprenylated benzophenones is associated with induction of the endoplasmic reticulum response. *Int J Cancer* **123**.

Przytycki PF, Singh M. 2020. Differential Allele-Specific Expression Uncovers Breast Cancer Genes Dysregulated by Cis Noncoding Mutations. *Cell Syst* **10**: 193–203.

Qin Y, Li B, Arumugam S, Lu Q, Mankash SM, Li J, Sun B, Li J, Flavell RA, Li HB, et al. 2021. m6A mRNA methylation-directed myeloid cell activation controls progression of NAFLD and obesity. *Cell Rep* **37**.

Querido E, Sfeir A, Chartrand P. 2020. Imaging of Telomerase RNA by Single-Molecule Inexpensive FISH Combined with Immunofluorescence. *STAR Protoc* **1**.

Rittenhouse KD, Johnson TR, Vicini P, Hirakawa B, Kalabat D, Yang AH, Huang W, Basile AS. 2013. RTP801 gene expression is differentially upregulated in retinopathy and is silenced by PF-04523655, a 19-mer siRNA directed against RTP801. *Investig Ophthalmol Vis Sci* **55**.

Rizzotto D, Zaccara S, Rossi A, Galbraith MD., Andrysik Z, Pandey A, Sullivan KD., Quattrone A, Espinosa JM., Dassi E, et al. 2020. Nutlin-Induced Apoptosis is Specified by a Translation Program Regulated by PCBP2 and DHX30. *Cell Rep* **30**: 1–15.

Robichaud N, Sonenberg N, Ruggero D, Schneider RJ. 2019. Translational control in cancer. *Cold Spring Harb Perspect Biol* **11**.

Romanel A, Lago S, Prandi D, Sboner A, Demichelis F. 2015. ASEQ: Fast allele-specific studies from next-generation

sequencing data. *BMC Med Genomics* **8**.

Sagara Y, Fernandez-Belda F, De Meis L, Inesi G. 1992. Characterization of the inhibition of intracellular Ca2+ transport ATPases by thapsigargin. *J Biol Chem* **267**.

Sato K, Akiyama M, Sakakibara Y. 2021. RNA secondary structure prediction using deep learning with thermodynamic integration. *Nat Commun* **12**.

Schafer S, Adami E, Heinig M, Rodrigues KEC, Kreuchwig F, Silhavy J, Van Heesch S, Simaite D, Rajewsky N, Cuppen E, et al. 2015. Translational regulation shapes the molecular landscape of complex disease phenotypes. *Nat Commun* **6**.

Schug J. 2008. Using TESS to predict transcription factor binding sites in DNA sequence. *Curr Protoc Bioinforma* unit 2.6.

Schupp M, Chen F, Briggs ER, Rao S, Pelzmann HJ, Pessentheiner AR, Bogner-Strauss JG, Lazar MA, Baldwin D, Prokesch A. 2013. Metabolite and transcriptome analysis during fasting suggest a role for the p53-Ddit4 axis in major metabolic tissues. *BMC Genomics* **14**.

Sengupta S, Peterson TR, Sabatini DM. 2010. Regulation of the mTOR Complex 1 Pathway by Nutrients, Growth Factors, and Stress. *Mol Cell* **40**.

Sofer A, Lei K, Johannessen CM, Ellisen LW. 2005. Regulation of mTOR and Cell Growth in Response to Energy Stress by REDD1. *Mol Cell Biol* **25**.

Song L, Chen Z, Zhang M, Zhang M, Lu X, Li C, Miao L. 2021. DDIT4 overexpression associates with poor prognosis in lung adenocarcinoma. *J Cancer* **12**.

St. Pierre CL, Macias-Velasco JF, Wayhart JP, Yin L, Semenkovich CF, Lawson HA. 2022. Genetic, epigenetic, and environmental mechanisms govern allele-specific gene expression. *Genome Res* **32**.

Suzuki K, Bose P, Leong-Quong RY, Fujita DJ, Riabowol K. 2010. REAP: A two minute cell fractionation method. *BMC Res Notes* **3**.

Tiu GC, Kerr CH, Forester CM, Krishnarao PS, Rosenblatt HD, Raj N, Lantz TC, Zhulyn O, Bowen ME, Shokat L, et al. 2021. A p53-dependent translational program directs tissue-selective phenotypes in a model of ribosomopathies. *Dev Cell* **56**.

Valentini S, Fedrizzi T, Demichelis F, Romanel A. 2019. PaCBAM: Fast and scalable processing of whole exome and targeted sequencing data. *BMC Genomics* **20**.

Valentini S, Gandolfi F, Carolo M, Dalfovo D, Pozza L, Romanel A. 2022. Polympact: Exploring functional relations among common human genetic variants. *Nucleic Acids Res* **50**.

Valentini S, Marchioretti C, Bisio A, Rossi A, Zaccara S, Romanel A, Inga A. 2021. TranSNPs: A class of functional SNPs affecting mRNA translation potential revealed by fraction-based allelic imbalance. *iScience* **24**.

Wang S, Konorev EA, Kotamraju S, Joseph J, Kalivendi S, Kalyanaraman B. 2004. Doxorubicin induces apoptosis in normal and tumor cells via distinctly different mechanisms: Intermediacy of H2O2- and p53-dependent pathways. *J Biol Chem* **279**.

Wang ZY, Leushkin E, Liechti A, Ovchinnikova S, Mößinger K, Brüning T, Rummel C, Grützner F, Cardoso-Moreira M, Janich P, et al. 2020. Transcriptome and translatome co-evolution in mammals. *Nature* **588**: 642–647.

Wayment-Steele HK, Kladwang W, Strom AI, Lee J, Treuille A, Becka A, Das R. 2022. RNA secondary structure packages evaluated and improved by high-throughput experiments. *Nat Methods* **19**.

White RM, Sessa A, Burke C, Bowman T, LeBlanc J, Ceol C, Bourque C, Dovey M, Goessling W, Burns CE, et al. 2008. Transparent Adult Zebrafish as a Tool for In Vivo Transplantation Analysis. *Cell Stem Cell* **2**.

Whitney ML, Jefferson LS, Kimball SR. 2009. ATF4 is necessary and sufficient for ER stress-induced upregulation of REDD1 expression. *Biochem Biophys Res Commun* **379**.

Wilks C, Zheng SC, Chen FY, Charles R, Solomon B, Ling JP, Imada EL, Zhang D, Joseph L, Leek JT, et al. 2021. recount3: summaries and queries for large-scale RNA-seq expression and splicing. *Genome Biol* **22**.

Xu Y, Ruggero D. 2020. The Role of Translation Control in Tumorigenesis and Its Therapeutic Implications. *Annu Rev Cancer Biol* **4**.

Yang B, Xu B, Yang R, Fu J, Li L, Huo D, Chen J, Yang X, Tan C, Chen H, et al. 2022. Long Non-coding Antisense RNA DDIT4-AS1 Regulates Meningitic Escherichia coli-Induced Neuroinflammation by Promoting DDIT4 mRNA Stability. *Mol Neurobiol* **59**.

Yang X, Liu QL, Xu W, Zhang YC, Yang Y, Ju LF, Chen J, Chen YS, Li K, Ren J, et al. 2019. m6A promotes R-loop formation to facilitate transcription termination. *Cell Res* **29**.

Yoshida T, Mett I, Bhunia AK, Bowman J, Perez M, Zhang L, Gandjeva A, Zhen L, Chukwueke U, Mao T, et al. 2010. Rtp801, a suppressor of mTOR signaling, is an essential mediator of cigarette smoke-induced pulmonary injury and emphysema. *Nat Med* **16**.

Zhang J, Chen X. 2008. Posttranscriptional Regulation of p53 and its Targets by RNABinding Proteins. *Curr Mol Med* **8**.

Zhou Y, Zeng P, Li YH, Zhang Z, Cui Q. 2016. SRAMP: Prediction of mammalian N6-methyladenosine (m6A) sites based on sequence-derived features. *Nucleic Acids Res* **44**.

Zuccotti P, Peroni D, Potrich V, Quattrone A, Dassi E. 2020. Hyperconserved Elements in Human 5′UTRs Shape Essential Post-transcriptional Regulatory Networks. *Front Mol Biosci* **7**.